








Protoplanetary Disk Rings as Sites for Planetesimal Formation

Daniel Carrera¹ , Jacob B. Simon^{1,2,3} , Rixin Li⁴ , Katherine A. Kretke³ , and Hubert Klahr⁵ 

¹Department of Physics and Astronomy, Iowa State University, Ames, IA 50010, USA; dcarrera@gmail.com

²JILA, University of Colorado and NIST, 440 UCB, Boulder, CO 80309, USA

³Department of Space Studies, Southwest Research Institute, Boulder, CO 80302, USA

⁴Department of Astronomy and Steward Observatory, University of Arizona, 933 North Cherry Avenue, Tucson, AZ 85721, USA

⁵Max-Planck-Institut für Astronomie: Heidelberg, Baden-Württemberg, Germany

Received 2020 September 13; revised 2020 December 13; accepted 2020 December 16; published 2021 January 29

Abstract

Axisymmetric dust rings are a ubiquitous feature of young protoplanetary disks. These rings are likely caused by pressure bumps in the gas profile; a small bump can induce a traffic-jam-like pattern in the dust density, while a large bump may halt radial dust drift entirely. The resulting increase in dust concentration may trigger planetesimal formation by the streaming instability (SI), as the SI itself requires some initial concentration of dust. Here we present the first 3D simulations of planetesimal formation in the presence of a pressure bump modeled specifically after those seen by Atacama Large Millimeter/submillimeter Array. We place a pressure bump at the center of a large 3D shearing box, along with an initial solid-to-gas ratio of $Z = 0.01$, and we include both particle back-reaction and particle self-gravity. We consider millimeter-sized and centimeter-sized particles separately. For simulations with centimeter-sized particles, we find that even a small pressure bump leads to the formation of planetesimals via the SI; a pressure bump does *not* need to fully halt radial particle drift for the SI to become efficient. Furthermore, pure gravitational collapse via concentration in pressure bumps (such as would occur at sufficiently high concentrations and without the SI) is not responsible for planetesimal formation. For millimeter-sized particles, we find tentative evidence that planetesimal formation does not occur. If this result is confirmed at higher resolution, it could put strong constraints on where planetesimals can form. Ultimately, our results show that for centimeter-sized particles planetesimal formation in pressure bumps is extremely robust.

Unified Astronomy Thesaurus concepts: Planet formation (1241); Planetesimals (1259); Protoplanetary disks (1300); Planetary system formation (1257)

1. Introduction

One of the major open questions in planet formation theory is how planetesimals (bodies 10–100 km in size) form out of millimeter- to centimeter-sized dust grains and pebbles. While collisions of micron- to millimeter-sized silicate grains generally lead to sticking, once particles reach millimeter to centimeter sizes and collision speeds reach $\Delta v_{\text{crit}} \sim 1 \text{ m s}^{-1}$, collisions typically lead to bouncing or fragmentation (e.g., Güttler et al. 2010; Zsom et al. 2010; Weidling et al. 2012; Kothe et al. 2013). Given that typical turbulent velocities inside a protoplanetary disk are much larger than Δv_{crit} (Ormel & Cuzzi 2007), planetesimals cannot grow by sticking of silicate particles. Some authors have suggested that icy aggregates are more sticky and can grow to larger sizes (Wada et al. 2009; Gundlach & Blum 2015), but recent experiments suggest that this is only true within a very narrow temperature range of 175–200 K (Musiolik & Wurm 2019). For particles whose growth is not limited by bouncing or fragmentation, competition between particle growth and rapid radial drift also conspires to limit particles to the millimeter to centimeter size range, depending on the particle’s location in the disk (Weidenschilling 1977; Birnstiel et al. 2012).

A promising mechanism to circumvent these barriers emerges when one accounts for both the aerodynamic drag and the momentum feedback onto the gas from the particles. The streaming instability (SI) is a radial convergence of particle drift that begins with a linear growth phase (Youdin & Goodman 2005; Youdin & Johansen 2007; Squire & Hopkins 2020), followed by a nonlinear phase that causes a rapid concentration of particles into mostly axisymmetric

filaments with a greatly enhanced density (e.g., Johansen & Youdin 2007; Johansen et al. 2007; Bai & Stone 2010a; Li et al. 2018; Abod et al. 2019). If the particle density exceeds the Roche density,

$$\rho_{\text{roche}} = \frac{9\Omega^2}{4\pi G}, \quad (1)$$

where Ω is the orbital frequency, then self-gravity between particles overpowers tidal forces. The resulting gravitationally bound clumps form with properties similar to solar system asteroids and Kuiper Belt Objects (Johansen et al. 2007, 2012, 2015; Simon et al. 2016, 2017; Schäfer et al. 2017; Abod et al. 2019; Li et al. 2019; Nesvorný et al. 2019); planetesimals are born.

For the SI to operate, however, requires that the solid-to-gas ratio, $Z = \Sigma_{\text{solid}}/\Sigma_{\text{gas}}$, be sufficiently large.⁶ The critical Z value needed to trigger the SI depends on the size of the particle stopping time, but in general $Z_{\text{crit}} > 0.02$, and Z_{crit} rapidly increases for smaller particles. More quantitatively and under reasonable assumptions for the disk conditions at 1 au, $Z_{\text{crit}} \sim 0.02$ is needed for the SI to produce filaments for meter-sized particles, and ~ 0.03 – 0.04 for small millimeter-sized grains (Carrera et al. 2015; Yang et al. 2017), though it is worth noting that Gerbig et al. (2020) have recently argued that Z_{crit} is also proportional to the Toomre Q parameter (Toomre 1964), so that Z_{crit} is lower for young massive disks. For reasonable

⁶ The SI is most effective when all the solids are in centimeter- to decimeter-sized pebbles. Since in all our simulations we used a single particle size, we will not distinguish between a solid-to-gas ratio and a “pebble-to-gas” ratio.

protoplanetary disk properties, however, such conditions are not regularly satisfied, and thus a mechanism is required to enhance Z , either globally (e.g., through photoevaporation of disk gas; Carrera et al. 2017) or locally via dust pileups at the snowline (e.g., Ida & Guillot 2016; Drazkowska & Alibert 2017; Schoonenberg & Ormel 2017) or local pressure bumps (the focus of this paper).

In recent years, the Atacama Large Millimeter/submillimeter Array (ALMA) has revealed a vast diversity of structures in nearby protoplanetary disks. Perhaps the most salient feature is a series of axisymmetric rings observed in the continuum emission associated with dust grains (ALMA Partnership et al. 2015; Andrews et al. 2018). These radial concentrations of dust are thought to be caused by axisymmetric enhancements in gas pressure, or “pressure bumps,” which may reduce or perhaps even reverse the direction of radial drift of solid particles (Whipple 1972). These structures may be the key ingredient required to enhance Z to sufficient values such that the SI is activated and planetesimals can form. This is especially true if planetesimal formation happens sufficiently early such that photoevaporation is quite unlikely to be the relevant mechanism for increasing Z and kick-starting the SI (see arguments in Carrera et al. 2017).

As discussed earlier, the key threshold that determines whether planetesimals form is that the mutual gravitational attraction between particles overpowers other forces. In the absence of significant velocity dispersion of these particles, gravitational collapse occurs when the enhanced density associated with particle clumping reaches the Roche density. The SI is perhaps the most promising route toward this critical collapse phase, but it may not be the only route. If solid particles can be sufficiently concentrated via other means, then the Roche density might be reached without the SI. As part of our investigation, we will explore whether pressure bumps that enhance Z enough to trigger the SI may in fact by-pass the SI altogether and produce planetesimals via gravitational instability (GI) within the pressure bump.

In addition to the question of *how* planetesimals form in pressure bumps (if at all), there are a number of other related questions we need to address in order to build a more complete understanding of planetesimal formation. First, do particles need to be *trapped* in a pressure bump (e.g., their radial drift halted), or will a weaker, transient enhancement in particle density as particles move through the bump suffice in producing planetesimals? Answering this question will be key to understanding how robust planetesimal formation is and which bump-inducing mechanisms (e.g., planets, magnetically induced zonal flows; Johansen et al. 2009) are likely to form planetesimals.

Second, where in relation to the pressure bump do planetesimals form? Do they form at the point of minimum radial drift, or elsewhere? If there is a pressure trap, at the exact center of the trap there is no headwind and the SI cannot be active (though the GI could be). Addressing this question will be crucial toward further developing planet formation models that make assumptions as to when and where planetesimals may form with respect to pressure bumps (e.g., Stammerl et al. 2019; Eriksson et al. 2020).

Finally, momentum feedback from particles within the pressure bump will influence the shape and structure of the bump in ways that are not yet clear. In turn, the potential deformation of the bump will likely itself influence the

planetesimals that do form as a result. This last question was first addressed in the work of Taki et al. (2016); they performed a 2D (radial-vertical) simulation of the vicinity of a radial pressure bump and found that the pressure bump is completely deformed by the particle back-reaction. They further found that the direct collapse of particles into planetesimals (i.e., by pure GI) is inhibited by this bump deformation, whereas the SI was active. Some key limitations of this work include the omission of stellar vertical gravity, particle self-gravity, and an azimuthal component to the simulations. Onishi & Sekiya (2017) corrected the first problem with a new 2D simulation that included vertical gravity. Because they allow dust particles to sediment, they found that the back-reaction is only a significant force in the thin dust layer at the midplane, where the particle density is high, and the majority of the pressure bump is largely unaffected.

A common feature of Taki et al. (2016) and Onishi & Sekiya (2017) is that the mechanism responsible for creating the pressure bump is assumed to be no longer active. In contrast, our investigation is more focused on the scenario where the external force that created the bump is still actively reinforcing the bump, though we do include some simulations where there is no external reinforcement, and for these cases we will make a direct comparison with previous work.

Our paper is organized as follows. In Section 2 we give a brief review on radial drift, particularly within the context of pressure bumps. Then, in Section 3 we summarize the numerical algorithms implemented in the ATHENA code, followed by a description of the experimental setup and initial conditions in Section 4. Our results are presented in Section 5. In Section 6 we discuss model uncertainties. Finally, we summarize and conclude in Section 7.

2. Review of Radial Drift and Pressure Bumps

Solid particles in the disk experience aerodynamic drag. The stopping time for a particle with mass m and material density ρ_s is given by

$$t_{\text{stop}} = \frac{m v_{\text{rel}}}{F_{\text{drag}}} = \frac{\rho_s a}{\rho c_s} \sqrt{\frac{\pi}{8}}, \quad (2)$$

where ρ is the gas density, a is the particle radius, ρ_s is the density of the solid material, and c_s is the isothermal sound speed. The stopping time is typically expressed as the dimensionless Stokes number $\tau \equiv t_{\text{stop}} \Omega$, where Ω is the Keplerian frequency. The dominant Stokes number in a disk is set by various growth barriers (Birnstiel et al. 2012). It turns out that in our simulations the particle size should be in the fragmentation-limited regime,

$$\tau_{\text{frag}} \approx \frac{v_{\text{frag}}^2}{\alpha c_s^2}, \quad (3)$$

where v_{frag} is the velocity at which particle collisions lead to fragmentation. For a fragmentation speed of $v_{\text{frag}} \sim 1\text{--}2 \text{ m s}^{-1}$, low turbulence ($\alpha = 10^{-4}$), and $c_s \approx 370 \text{ m s}^{-1}$ from our disk model (described in Section 4.1), we get $\tau_{\text{frag}} \sim 0.07\text{--}0.3$. The centimeter-sized (millimeter-sized) particles that we choose for our simulations (see Section 4.5) correspond to $\tau \approx 0.12$ (0.012); thus, our chosen particle sizes are consistent with this fragmentation limit.

The millimeter to centimeter size range is also consistent with recent dust coagulation models in the vicinity of a pressure bump. In Stammler et al. (2019), the particle sizes are drift limited in the vicinity of the pressure bump and only grow to the fragmentation limit at the center of the bump. While their pressure bump is not an exact analog of ours (e.g., different shape, different location), it is worth noting that near the bump the typical particle size goes from around 1 mm near the peak to ~ 2 cm at the peak.

For a locally isothermal disk (i.e., one with c_s only dependent on the radial direction), hydrostatic equilibrium dictates that the vertical gas density profile must follow a Gaussian distribution with scale height $H = c_s/\Omega$.

The gas also experiences pressure support in the radial direction, as a result of the global temperature gradient. As a result, the gas orbits at a slightly sub-Keplerian speed. The difference between the Keplerian speed, v_k , and the azimuthal speed of the gas, u_ϕ , results in solid particles experiencing a small headwind,

$$\Delta v \equiv v_k - u_\phi = \eta v_k, \quad (4)$$

where η is given by Nakagawa et al. (1986) as

$$\eta = -\frac{1}{2} \left(\frac{c_s}{v_k} \right)^2 \frac{d \ln P}{d \ln r}. \quad (5)$$

For scale-free numerical simulations it is helpful to scale the headwind Δv by the sound speed

$$\Pi \equiv \frac{\Delta v}{c_s} = -\frac{1}{2} \left(\frac{c_s}{v_k} \right) \frac{d \ln P}{d \ln r}. \quad (6)$$

As solid particles experience a headwind, aerodynamic drag leads to the gradual loss of angular momentum, causing the solids to gradually drift toward the star. The rate of radial drift is

$$v_{\text{drift}} = -\frac{2 \Delta v}{\tau + \tau^{-1}} = -\frac{2 \eta v_k}{\tau + \tau^{-1}}. \quad (7)$$

Note that the rate of radial drift is proportional to the logarithmic pressure gradient,

$$v_{\text{drift}} \propto \frac{d \ln P}{d \ln r}. \quad (8)$$

If the disk has a pressure bump, the “downstream” side of the bump (i.e., toward the star) will have reduced $d \ln P/d \ln r$, leading to slower radial drift. This would create an overdensity of particles, somewhat analogous to a traffic jam. If $d \ln P/d \ln r = 0$, particle drift stops entirely at that point, so that it becomes a particle trap. Such concentration of particles may be a critical step for triggering planetesimal formation by the SI (Carrera et al. 2015; Yang et al. 2017). Regardless of the process that concentrates particles, once the particle density reaches the Roche density, the particle self-gravity overwhelms the Keplerian shear and the particles form a gravitationally bound clump, which will (upon further collapse) form planetesimals.

3. Numerical Methods

For those readers familiar with our previous works, feel free to read the following short text, skip the rest of Section 3, and continue on to Section 4: we conduct a series of local, shearing box simulations with the ATHENA gas+particle code (ignoring

magnetic fields and imposing no externally driven disk turbulence). The gas is treated as a compressible, isothermal fluid, and the particles are treated via the superparticle approach. Particle self-gravity is implemented using a particle-mesh approach with shearing-periodic radial boundary conditions.

3.1. Hydrodynamic Solver

We use the ATHENA code in pure hydrodynamic mode with particle–gas interactions included and neglecting magnetic fields. We employ the local, shearing box approximation, in which we simulate a disk patch of sufficiently small size compared to the radial distance, R_0 , from the central object that curvature effects can be neglected (though see Section 4.4 for a description of why this may not be strictly true in our case). As such, the shearing box is a local Cartesian frame (x, y, z) , which is defined in terms of the disk’s cylindrical coordinate system (R, ϕ, z') as $x = (R - R_0)$, $y = R_0 \phi$, and $z = z'$. This box is corotating around the central object with an angular velocity Ω , defined at the center of the box, R_0 . More details of the shearing box algorithm and its implementation can be found in Hawley et al. (1995) and (with respect to ATHENA) Stone & Gardiner (2010). Within this approximation, the equations of gas dynamics are

$$\frac{\partial \rho}{\partial t} + \nabla \cdot (\rho \mathbf{u}) = 0, \quad (9)$$

$$\begin{aligned} \frac{\partial \rho \mathbf{u}}{\partial t} + \nabla \cdot (\rho \mathbf{u} \mathbf{u} + P \mathbf{I}) &= 2q\rho\Omega^2 \mathbf{x} - \rho\Omega^2 \mathbf{z} \\ &\quad - 2\Omega \times \rho \mathbf{u} + \rho_p \frac{\mathbf{v} - \mathbf{u}}{t_{\text{stop}}}. \end{aligned} \quad (10)$$

Here \mathbf{u} is the gas velocity and \mathbf{I} is the identity matrix. The shear parameter q is defined as $q = -d \ln \Omega/d \ln r$, so that $q = 3/2$ for a Keplerian disk. From left to right, the source terms in Equation (10) correspond to radial tidal forces (gravity and centrifugal), vertical gravity, the Coriolis force, and the particle momentum feedback onto the gas. In this last term, ρ_p is the mass density of solid particles. The particle velocity vector is \mathbf{v} , and t_{stop} is the particle stopping time—the timescale over which a particle will lose a factor of e of its momentum due to gas drag. This feedback term is initially calculated at the particle locations and then distributed to the gas grid cells; we describe this mapping in more detail below. We also supplement these equations with an isothermal equation of state $P = \rho c_s^2$, where c_s is the isothermal sound speed.

A second-order-accurate Godunov flux-conservative method, coupled with the dimensionally unsplit corner transport upwind method of Colella (1990) and the third order in space piecewise parabolic method of Colella & Woodward (1984), is used to solve the left-hand side of these equations (i.e., ignoring source terms). A more detailed description and tests of these algorithms can be found in Gardiner & Stone (2005, 2008) and Stone et al. (2008). Additional algorithms are used to integrate these equations within the shearing box approximation, thus handling the noninertial source terms. These include orbital advection (the background Keplerian velocity is subtracted and integrated analytically; Masset 2000; Johnson et al. 2008a, 2008b) and Crank–Nicolson differencing, which is used to preserve epicyclic energy to machine precision. A detailed description of these algorithms, their

implementation, and test problems are found in Stone & Gardiner (2010).

ATHENA includes a superparticle approach in which each superparticle is a statistical representation of a number of smaller particles. Superparticle i (hereafter “particle” for simplicity) is governed by an equation of motion:

$$\frac{dv'_i}{dt} = 2(v'_{iy} - \eta v_k) \Omega \hat{x} - (2 - q)v'_{ix} \Omega \hat{y} - \Omega^2 z \hat{z} - \frac{v'_i - \mathbf{u}'}{t_{\text{stop}}} + \mathbf{F}_g. \quad (11)$$

In the above equation, the prime denotes a frame in which the background shear velocity has been subtracted, i.e., the orbital advection scheme mentioned above. From left to right, the source terms are radial acceleration of the particles due to the Coriolis effect, the gravitational and centrifugal forces, and radial drift; azimuthal motion due to the Coriolis effect; vertical motion due to the central star’s gravity; gas drag; and the force due to particle self-gravity.

The ηv_k term is responsible for inward radial drift due to aerodynamic drag (see Section 2 and Equation (7)); we follow Bai & Stone (2010c) and impose an inward force on the particles in the form of the ηv_k term. In practice, this means that the azimuthal velocities of particles and gas are shifted to slightly higher values (by ηv_k) than would be present in a real disk. Hence, we are allowed to maintain a Keplerian gas velocity profile as described above, and the particles are actually boosted to super-Keplerian speed. This approach allows us to capture the essential physics of differential gas-particle motion.

Following Bai & Stone (2010c), Equation (11) is solved with a semi-implicit integration and a triangular-shaped cloud (TSC) scheme that maps the particle momentum feedback to the grid cell centers (as mentioned above) and inversely interpolates the gas velocity to the particle locations (this interpolated quantity is \mathbf{u}'). More details of this algorithm, in addition to test problems, can be found in Bai & Stone (2010c).

3.2. Particle Self-gravity

All of our simulations include particle self-gravity, with a corresponding force in the equation of motion represented by \mathbf{F}_g . This term is found by solving Poisson’s equation for particle self-gravity, and we use the same methods employed in Simon et al. (2016). Briefly, we use the TSC scheme (mentioned above) to map the mass density of particles to grid cell centers. We shift the radial boundaries to be purely periodic, and we use a fast Fourier transform (FFT) to solve the Poisson equation for the gravitational potential,

$$\nabla^2 \Phi = 4\pi G \rho_p. \quad (12)$$

Finally, the self-gravity force is $\mathbf{F}_g = -\nabla \Phi$ (see Simon et al. 2016; Hawley et al. 1995, for more details). We employ open vertical boundaries for the potential, and as such, we apply a Green’s function method to the Poisson equation in the vertical dimension (see Koyama & Ostriker 2009; Simon et al. 2016). We then calculate the force due to self-gravity by applying a central finite difference, after which we interpolate this force (which is located at the grid cell centers) to the locations of the particles via TSC. We have tested this algorithm in our

previous work (Simon et al. 2016), and more details can be found there.

3.3. Boundary Conditions

The boundary conditions are the same for both the gas and particle components: shearing-periodic in the radial dimension (Hawley et al. 1995), purely periodic in azimuth, and a modified outflow boundary in the vertical dimension in which gas density is extrapolated into the ghost zones using an exponential function (Simon et al. 2011; Li et al. 2018). This extrapolation has been shown to reduce gas mass loss and spurious effects near the vertical boundaries for vertically stratified shearing box simulations (Simon et al. 2011).

The modified outflow boundary condition will not entirely prevent gas mass loss along the vertical boundary, however, and to ensure that mass is globally conserved throughout our domain, we renormalize the gas density in every cell at every time step to keep the total gas mass constant. As for the particles’ component, we verify that no particles escape the simulation box through the vertical boundaries.

The gravitational potential has the same boundary conditions in the radial and azimuthal directions as the gas and particles. However, the vertical boundary conditions are open, with the potential in the ghost zones calculated via a third-order extrapolation.

4. Simulation Setup

Up until now, simulations of the SI have relied on small simulation domains and highly idealized initial conditions, such as a significantly enhanced solid-to-gas ratio. This was a result of computational cost and the need to explore a large and unfamiliar parameter space.

Here we present large-scale simulations with conditions grounded in recent observations of nearby circumstellar disks. Specifically, we model a large slice of a protoplanetary disk with an embedded axisymmetric pressure bump comparable to those responsible for observed dust rings. Generally, the gas structure that produces these dust rings is not well known. However, Rosotti et al. (2020) recently estimated the width of gas rings around a K-type (AS 209) and A-type (HD 163296) star, and they found $w/r \sim 7\%$ and $w/r \sim 22\%$, respectively, where w is the standard deviation of a Gaussian density profile.

To set up our bump properties, we assume a specific disk model that is loosely based on HL Tau (see below). In particular, we consider a pressure bump located at $r_p = 50$ au, making it comparable to HL Tau’s ring at 49 au (B49; ALMA Partnership et al. 2015). We choose a ring with FWHM = 12 au, which is equivalent to $w/r \approx 10\%$, in approximate agreement with the gas ring widths mentioned above.

4.1. Disk Model

For our disk model, we assume a stellar mass of $M_* = 1M_\odot$ and a disk mass of $M_{\text{disk}} = 0.09M_\odot$. We model the disk surface density via a simple power law,

$$\Sigma(r) = \frac{M_{\text{disk}}}{2\pi r_c} r^{-1}, \quad (13)$$

where r is the distance to the star and $r_c = 200$ au. We also assume a simple power-law dependence for the gas

temperature, consistent with an optically thin disk

$$T(r) = 280 \text{ K} \left(\frac{r}{\text{au}} \right)^{-1/2}. \quad (14)$$

With this temperature profile, the disk aspect ratio is

$$\frac{H}{r} = \frac{c_s}{v_k} = 0.033 \left(\frac{r}{\text{au}} \right)^{1/4}. \quad (15)$$

Next, using the isothermal approximation $P = c_s^2 \rho$, with $c_s \propto \sqrt{T}$, we obtain the background pressure profile,

$$P(r) = c_s^2 \rho \propto T \frac{\Sigma}{H} \propto r^{-11/4}. \quad (16)$$

Combining $d \ln P / d \ln r = -11/4$ with Equation (15), we obtain the headwind parameter,

$$\Pi(r) = 0.046 \left(\frac{r}{\text{au}} \right)^{1/4} \quad (17)$$

and

$$\eta = 1.6 \times 10^{-3} \left(\frac{r}{\text{au}} \right)^{1/2}. \quad (18)$$

4.2. Pressure Bump and Rossby Wave Instability

We model the pressure bump as a Gaussian in the gas density and pressure as follows:

$$\rho(x, y, z) = \rho_0 [1 + A e^{(-x^2/2w^2)}] e^{(-z^2/2H^2)}, \quad (19)$$

where A is the dimensionless amplitude of the bump, w is the bump width, H is the vertical gas scale height, and x is the radial coordinate, centered at the peak of the pressure bump. Note that we include an additional Gaussian term in z as well, which accounts for vertical hydrostatic equilibrium in an isothermal gas.

Since the amplitude of pressure bumps is not well constrained by observations, we leave A as a free parameter in our study. However, a sufficiently large amplitude (for a given width) will render the system unstable to the Rossby wave instability (RWI; Lovelace et al. 1999).⁷ Assuming a constant surface density (i.e., no r dependence on Σ), Ono et al. (2016) derive a criterion for the maximum amplitude of a pressure bump that is stable against the RWI, as a function of the bump width. In the case of a Gaussian bump for an isothermal disk with $H/r = 0.1$ (case iv in their paper; most similar to our model) they find

$$A_{\text{MS}} = 1.06 \times 10^5 \left(\frac{w}{r} \right)^{5.72}, \quad (20)$$

where A_{MS} is the amplitude of marginal stability, w is the bump's width (i.e., the standard deviation of the Gaussian), and r is the semimajor axis of the bump. These coefficients are valid for $0.05 \leq w/r \leq 0.2$ (our model has $w/r \approx 0.1$). This stability criterion is shown in Figure 1.

As noted earlier, our pressure bump has an FWHM of 12 au and is placed at $r_p = 50$ au. At that semimajor axis, the disk scale height is $H = 4.5$ au. Expressed in terms of the scale

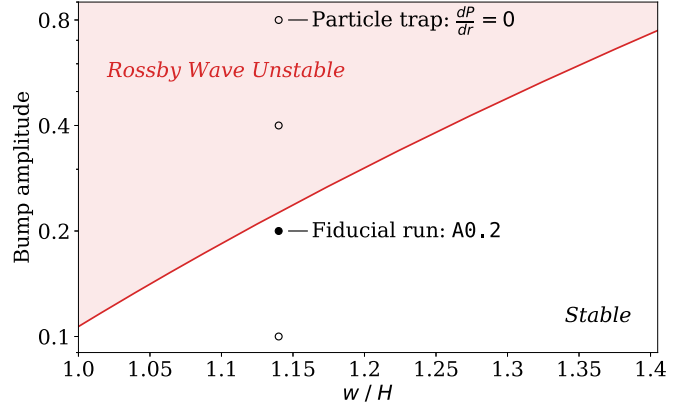


Figure 1. The red curve marks the maximum amplitude for a Gaussian pressure bump to be stable against the RWI as derived via Ono et al. (2016). The plot assumes a disk aspect ratio of $H/r = 0.09$, which corresponds to our simulation setup. All our simulations (marked as circles) have a pressure bump at 50 au with $w = 1.14H$.

height, a Gaussian with an FWHM of 12 au must have a standard deviation of $w = 1.14H$. Figure 1 shows the stability criterion of Ono et al. (2016) in terms of w/H . For $w = 1.14H$, the amplitude of a marginally stable bump is $A = 0.226$. However, a bump that size will never be able to completely halt particle migration since the pressure gradient dP/dr is always negative. A true particle trap ($dP/dr = 0$) requires a bump amplitude close to $A = 0.8$. Despite the potential role of the RWI in disrupting a pressure bump with such an amplitude, exploring the role of such an amplitude on planetesimal formation will further our understanding of the relevant physics. Furthermore, given the simplifications associated with the Ono et al. (2016) work (e.g., a constant radial surface density profile), a bump that traps drifting particles may still be quite stable to RWI under different conditions.

These considerations motivate the following exploration of the amplitude parameter:

1. $A = 0.2$, since that is close to the largest bump amplitude consistent with Rossby wave stability.
2. $A = 0.8$ to include one run with a particle trap.
3. $A = 0.1$ and 0.4 to explore parameter space. $A \in \{0.1, 0.2, 0.4, 0.8\}$ is uniform in log space.

The parameters for these bumps are shown in Figure 1.

To our knowledge, a study equivalent to Ono et al. (2016) but with more realistic surface density structures has not been performed. Thus, precisely which amplitudes in our parameter set are unstable to the RWI may change under more realistic conditions.

Finally, any long-lived pressure bump must be in geostrophic balance with the azimuthal flow. Integrating the momentum equation assuming such equilibrium and using Equation (19), we arrive at

$$u_y(x, y, z) = \frac{-A x c_s^2 e^{(-x^2/2w^2)}}{2w^2 \Omega [1 + A e^{(-x^2/2w^2)}]}. \quad (21)$$

4.3. Newtonian Relaxation

In the absence of particles, initializing the azimuthal gas speed according to Equation (21) would be enough to ensure that the bump remains stable. However, particle feedback will gradually disrupt the bump unless there is an external force to

⁷ In principle, the Rayleigh instability could set in, but as discussed in Li et al. (2000) and Ono et al. (2016), the stability condition for the RWI suffices to guarantee stability for the Rayleigh instability.

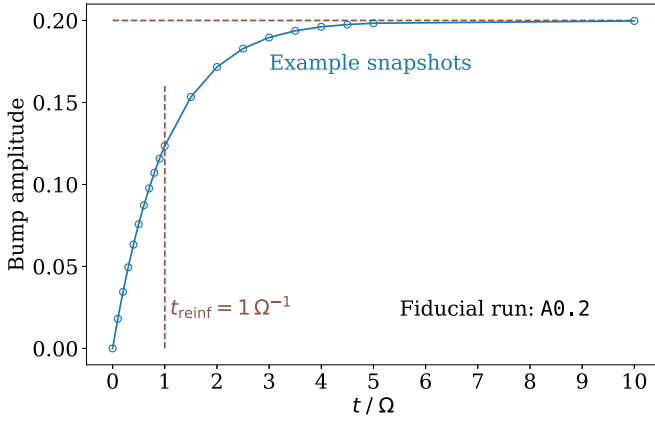


Figure 2. Amplitude of the pressure bump for our fiducial run, A0.2. Open circles mark simulation snapshots where the bump amplitude, $A = \max(\Sigma)/\min(\Sigma) - 1$, is calculated (Σ is the gas column density). The amplitude converges toward $A = 0.2$ after a few reinforcement timescales.

reinforce it. For this work we assume that there is indeed some unspecified force (e.g., a planet or a magnetically induced zonal flow; Johansen et al. 2009) that reinforces the pressure bump on some reinforcement timescale t_{reinf} . To simulate this process, we use Newtonian relaxation to adjust the radial profile of ρ and u_y ,

$$\Delta\rho = (\hat{\rho} - \rho) \frac{\Delta t}{t_{\text{reinf}}} \quad (22)$$

$$\Delta u_y = (\hat{u}_y - u_y) \frac{\Delta t}{t_{\text{reinf}}}, \quad (23)$$

where $\hat{\rho}$ and \hat{u}_y denote the values in Equations (19) and (21), respectively. To illustrate how a pressure bump develops under our Newtonian relaxation scheme, we show (Figure 2) the evolution of the pressure bump amplitude,

$$A(t) \equiv \frac{\max[\Sigma(t)]}{\min[\Sigma(t)]} - 1, \quad (24)$$

in one of our simulations. The simulation begins with a uniform gas density. The target density profile $\hat{\rho}$ is a Gaussian bump with amplitude $A = 0.2$ and standard deviation $w = 1.14H$, and the reinforcement timescale is $t_{\text{reinf}} = 1 \Omega^{-1}$. The figure shows the exponential convergence of the bump amplitude $A \rightarrow 0.2$.

4.4. Domain Size and Resolution

In order to encompass the entire width of the radial Gaussian and prevent spurious effects at the boundaries, we must choose a reasonably large radial domain size. We have found that $L_x = 9H$ is sufficiently large to avoid edge effects. In line with our previous works, we set the azimuthal extent of the domain to be $L_y = 0.2H$. We set the height to the domain to $L_z = 0.4H$ for runs with centimeter-sized particles and $L_z = 0.8H$ for millimeter-sized particles.⁸ This height ensures that no particles cross the vertical boundary and escape the domain.

Admittedly, $L_x = 9H$ is a long box that stretches the limits of the shearing box approximation. In particular, the length of this box normalized to its distance from the star is $L_x/2r_0 \approx 0.4$, clearly not satisfying the condition for the shearing box

approximation: the error terms in the shearing box come from Hill’s approximation. In the nonshearing frame we can write the equations of motion of particles as

$$\ddot{x} - 2\Omega\dot{y} = \Omega^2 \left[1 + x - \frac{1+x}{r^3} \right] + F_x \quad (25)$$

$$\approx \Omega^2 (3x - 3x^2 + 4x^3 - \dots) + F_x \quad (26)$$

$$\ddot{y} + 2\Omega\dot{x} = \Omega^2 \left[y - \frac{y}{r^3} \right] + F_y \quad (27)$$

$$\approx \Omega^2 (3xy - 6x^2y + 10x^3y - \dots) + F_y, \quad (28)$$

where (x, y) is the particle position normalized by r_0 , $\mathbf{r} = (1+x, y)$, and \mathbf{F} contains all other forces such as aerodynamic drag. For a shearing box like ours, where $L_x \gg L_y$, the largest error term is $E_x \approx -3x^2\Omega^2$. Since the leading term in Equation (26) is $3x\Omega^2$, the relative error is on the order of $|E_x/3x\Omega^2| \sim |x| \leq L_x/2r_0$. Thus, for the shearing box to be a reasonable approximation, $L_x/2r_0 \ll 1$. This is evidently not the case for our runs. However, we consider this an acceptable limitation because all of the relevant physics (aerodynamic drag, gas pressure, particle back-reaction, self-gravity) act on a very local scale ($\ll L_x$). In addition, the main alternative to a long shearing box (i.e., a global 3D simulation) is currently not feasible (in terms of both numerical resolution and code development).

Given the large domain size, computational expense dictates that a moderate resolution be employed. We use a standard resolution of 640 zones per H for nearly all of our simulations. The resolution of 640 zones per H is equivalent to the “SII28” simulations of Simon et al. (2016), which produced a reasonable number of planetesimals. Thus, with a standard domain size of $L_x \times L_y \times L_z = 9H \times 0.2H \times 0.4H$, our total resolution is $5760 \times 128 \times 256$. However, for the run with millimeter-sized particles we decrease the resolution to 320 zones per H in order to offset the cost of smaller time steps needed for small-particle runs and the greater vertical extent of the simulation domain. The total resolution for that run is $2880 \times 64 \times 256$. Finally, the total number of particles is the same as the number of grid cells— 1.89×10^8 particles for our standard resolution runs.

4.5. Initial Conditions and Parameters

To recap, all runs have a pressure bump centered at $r_p = 50$ au, with standard deviation $w = 1.14H$, and $H = 4.5$ au (Section 4.2). At this location, the headwind parameter (Equation (17)) is $\Pi = 0.12$. All simulations have a global dust-to-gas ratio of $Z = 0.01$ (a value comparable to that of the solar nebula) with no ab initio enhancement in the solid component. Simulations with an externally reinforced bump have a reinforcement timescale of $t_{\text{reinf}} = 1 \Omega^{-1}$.

Our simulations use “code units,” where $c_s = \Omega = H = 1$ define the units of length and time. For our disk model at 50 au, the relative strength of tidal forces to self-gravity (i.e., the standard \tilde{G} parameter in previous works, e.g., Simon et al. 2017; Abod et al. 2019) is

$$\tilde{G} \equiv \frac{4\pi G \rho_{\text{mid}}}{\Omega^2} \approx 0.2, \quad (29)$$

where ρ_{mid} is the midplane gas density of the unperturbed disk model. This corresponds to a gravitationally stable (in terms of

⁸ This larger vertical domain is required because the particle scale height will be higher for the millimeter-sized particles, thus leading to unacceptable mass loss from the domain.

Table 1
Our Nine Simulations

Run	Particle Size	Amplitude	RW Stable?	Resolution	Trap	Feedback	Reinforcement
A0.1	1 cm	0.10	✓	640/ H	×	✓	✓
A0.2	1 cm	0.20	✓	640/ H	×	✓	✓
A0.4	1 cm	0.40	×	640/ H	×	✓	✓
A0.8	1 cm	0.80	×	640/ H	✓	✓	✓
lores.1mm	1 mm	0.20	✓	320/ H	×	✓	✓
hires.1mm	1 mm	0.20	✓	640/ H	×	✓	✓
NoFeedback	1 cm	0.80	×	640/ H	✓	×	✓
R0.2	1 cm	0.20	✓	640/ H	×	✓	×
R0.8	1.6 cm	0.80	×	640/ H	✓	✓	×

Note. Our fiducial model, A0.2, has centimeter-sized particles and a pressure bump with amplitude $A = 0.2$. Pressure bumps with amplitude $A \leq 0.2$ are likely Rossby wave stable, but we simulate bumps up to $A = 0.8$ because that is the amplitude needed to form a particle trap with $dP/dr = 0$. We also carry out a run in which we remove the particle–gas feedback, two runs without pressure bump reinforcement (Section 4.3) so that the bump can dissipate by particle feedback, and two runs with millimeter-sized particles. Simulation R0.8 was unintentionally run with a slightly larger particle size.

the gas) disk with Toomre (Toomre 1964) $Q \approx 8$. For our simulations, the midplane gas density is $\rho_{\text{mid}} \approx \rho_0 \equiv 1$. In these units the Roche density is exactly $\rho_{\text{roche}} = 9\Omega^2/4\pi G = 9\rho_{\text{mid}}/\tilde{G} = 45$.

All simulations begin with a flat density profile in both the gas and solid components, with vertical stratification but no pressure bump,

$$\rho(x, y, z)|_{t=0} = \left[1 + \frac{\rho_0 A w \sqrt{2\pi}}{L_x} \right] e^{(-z^2/2H^2)}. \quad (30)$$

Then, the simulation is allowed to develop a pressure bump on its own. The scaling constant ensures that the midplane density $\rho(z=0)$ converges to a value close to ρ_0 at the edges of the box and toward $\rho_0(1+A)$ in the middle of the box.

One of the key parameters that controls the outcome of the SI is the dimensionless stopping time, or the Stokes number $\tau \equiv t_{\text{stop}}\Omega$ (where t_{stop} is defined via Equation (2); e.g., Carrera et al. 2015). Typical simulations of the SI assume that τ is constant, since particle and disk properties are assumed to be constant (e.g., Simon et al. 2016; Abod et al. 2019). However, in the presence of a pressure bump, ρ varies inside the simulation domain. So instead we assign the particle a fixed physical radius of either 1 cm or 1 mm and compute the Stokes number dynamically at every time step. For reference, a 1 cm particle has a Stokes number of $\tau \sim 0.12$ away from the pressure bump in our setup. In all simulations, we choose only a single particle size for simplicity. Multiple particle sizes may very well have an effect on our results (see Krapp et al. 2019), and we leave the study of including more particle species for future work.

4.6. List of Simulations

Altogether, we conducted nine simulations (which are also summarized in Table 1):

A0.2: Our fiducial run, with a fixed particle size of 1 cm, a pressure bump with an amplitude of $A = 0.2$, and at full resolution (640 zones/ H ; see Section 4.4).

A0.8: A full resolution run with centimeter-sized particles and a pressure bump amplitude of $A = 0.8$. While this bump may be Rossby wave unstable (see Section 4.2), it is important to quantify the effect of a particle trap ($d \ln P/d \ln r = 0$).

A0.1, A0.4: Two runs to complete the exploration of amplitude parameter space.

hires.1mm, lores.1mm: To investigate the effect of particle size, we run simulations with millimeter-sized particles. Due to the high computational cost, we cannot run long-term simulations of millimeter-sized particles at full 640/ H resolution. Instead, we do a short simulation at full resolution and a long-term simulation at half-resolution (320/ H).

NoFeedback: To test whether planetesimals form by the SI and not GI induced directly from particle concentration in the pressure trap, we run one simulation with the particle feedback (critical for the SI) turned off.

R0.2, R0.8: Lastly, we run two simulation that *begin* with a fully formed bump in geostrophic balance, but with no external reinforcement (see Section 4.3). Then, we measure how quickly the bump is destroyed by particle feedback and whether planetesimals can form before the bump dissipates.

5. Results

5.1. Particle Density and the Roche Density

Figure 3 shows the maximum particle density as a function of time for most of our runs. All models with centimeter-sized particles begin with an initial sedimentation phase that increases the maximum particle density $\rho_{p,\text{max}}$ for the first $\Delta t \sim 10 \Omega^{-1}$ of evolution. At that moment particle feedback begins to alter the velocity of the gas, so the NoFeedback simulation separates from the other models. For models A0.2–A0.8 it takes another $\Delta t \sim 10 \Omega^{-1}$ for the SI to form filaments with sufficient density to trigger self-gravity. The key result here is that all simulations with amplitude $A \geq 0.2$ and centimeter-sized particles achieved particle densities several orders of magnitude greater than the Roche density. Since model A0.8 is the only model with a particle trap (meaning that $\Delta v = 0$), we find that a particle trap is not needed to form planetesimals by the SI. Furthermore, a pressure bump that is Rossby wave stable (again, according to the criterion of Ono et al. 2016; model A0.2) is seen to trigger planetesimal formation.

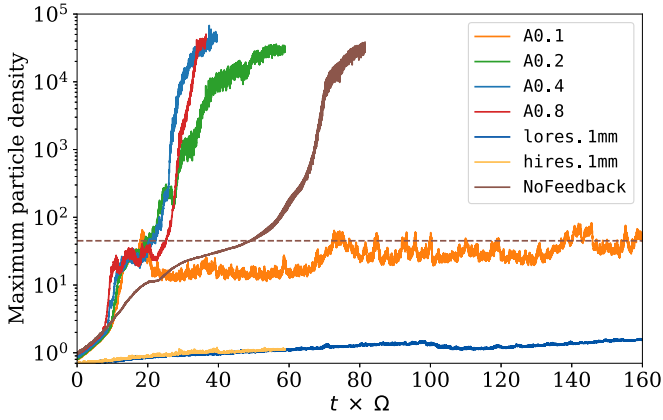


Figure 3. Maximum particle density $\rho_{p,\max}$ (in code units) vs. time. The dashed line marks the Roche density ρ_{roche} . Most models (A0.2–A0.8) go through three main stages: (1) initial sedimentation ($t \approx 0\text{--}10 \Omega^{-1}$), (2) the SI forms dense filaments that cross the Roche density, and (3) gravitational collapse of overdense regions into particle clumps. All simulations with $A > 0.1$ form gravitationally bound clumps. Simulations with millimeter-sized grains (lores.1mm and hires.1mm) have very slow density growth and may never reach the Roche density (see Section 5.5).

5.2. Comparison to a Simple Model

To develop some intuition as to why planetesimal formation is still possible, even without trapping, we consider a pressure bump that reaches a steady state with a constant particle mass flux and has no particle trap,

$$\dot{M}_p = 2\pi r \Sigma_p v_r = \text{const}, \quad (31)$$

where Σ_p is the particle surface density and v_r is the radial velocity. The pressure bump creates a localized reduction of v_r on the downstream side of the bump and a corresponding localized increase in Σ_p . In effect, there is a traffic jam of particles in the region where the particle drift is slowed down, and this traffic jam leads to a local enhancement in the solid-to-gas ratio. Figure 4 shows the solid-to-gas ratio Z predicted by the steady-state model for a pressure bump with $A = 0.2$. Note that, while v_r and \dot{M}_p clearly depend on the particle Stokes number, the particle density ($Z \propto \Sigma_p \propto \dot{M}_p / v_r$) is independent of τ . The steady-state model gives a peak solid-to-gas ratio of $Z_{\max} = 0.0139$, which is nearly identical to the critical Z_{crit} predicted by Yang et al. (2017) for centimeter-sized particles ($\tau \approx 0.12$) and much smaller than the $Z_{\text{crit}} = 0.025$ for millimeter-sized particles.

In other words, the steady-state model predicts that runs A0.4 and A0.8 should trigger strong clumping, that run A0.2 is marginal, and that runs A0.1 and *.1mm *should not* produce strong clumping. Considering all the simplifications, the simple steady-state model was surprisingly predictive.

5.3. Time and Location of Planetesimal Formation

When planetesimal formation does occur, it is rapid, requiring only a few tens of Ω^{-1} . The run with no particle feedback takes twice as long to cross the Roche density as the equivalent run with feedback (i.e., A0.8). We shall return to the role of feedback in Section 5.4.

Finally, the reader may notice that the simulations with no bump reinforcement (runs R0.2 and R0.8) are not shown in Figure 3. This is intentional. These runs begin with a fully

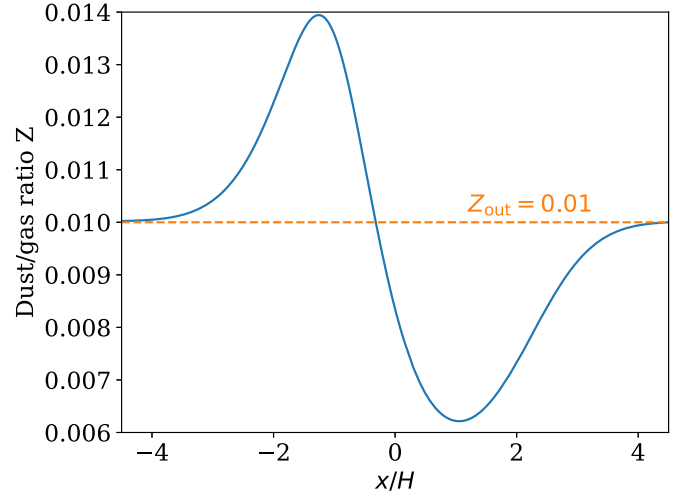


Figure 4. Solid-to-gas ratio Z implied by the simple steady-state model of Equation (31) for a pressure bump with amplitude $A = 0.2$. The peak solid-to-gas ratio is $Z_{\max} = 0.0139$, independent of τ . This is a borderline value for centimeter-sized particles ($\tau \approx 0.12$) and too small to clump particles for millimeter-sized particles (Yang et al. 2017).

formed pressure bump, which gives them a head start in planetesimal formation. We shall discuss these runs, as well as the effect of removing the bump reinforcement, in Section 5.7.

Figures 5–7 show snapshots of simulations A0.2, A0.4, and A0.8 at the time when bound particle clumps begin to form. The figures also show the headwind Δv , as well as the location of the particle trap ($\Delta v = 0$) for A0.8, or the location where Δv reaches its minimum value for A0.2 and A0.4. Some important takeaways include the following:

1. Planetesimal formation is not restricted to a fixed point in space. The planetesimal-forming filaments drift, and the particle clumps drift. In all cases, planetesimal formation is radially dispersed. Presumably, when clumps collapse into planetesimals, those will stop drifting, but our simulations cannot resolve the final collapse. The collapse itself is likely to be much faster (tens of years) than the orbital timescale at 50 au (Nesvorný et al. 2010; Wahlberg Jansson & Johansen 2014).
2. Even when a particle trap is present (run A0.8), planetesimal formation does not occur at the trap. In A0.4 particle clumps form before the minimum Δv , and in run A0.2 they form after. Compare this with Onishi & Sekiya (2017), who found that planetesimals formed at the particle traps. However, their run had a lower Π (0.05 vs. 0.12 for our runs), so that a bump with $A = 0.2$ formed a particle trap. Evidently there is an interplay between Π and A , and in principle planetesimal formation can occur on either side of the minimum Δv . The Δv needed to trigger the SI is some value > 0 ; run A0.4 must have reached this value before the minimum Δv .
3. In model A0.2 planetesimal formation is a much slower, more gradual process. Notice that in Figure 5 the snapshots are taken at intervals of $\Delta t = 15/\Omega$, while Figures 6 and 7 have snapshots taken at intervals of $\Delta t = 5/\Omega$.
4. Figure 5 suggests that simulation A0.2 might be a marginal case. The bound clumps form *after* the minimum Δv . The densest filament forms at the location

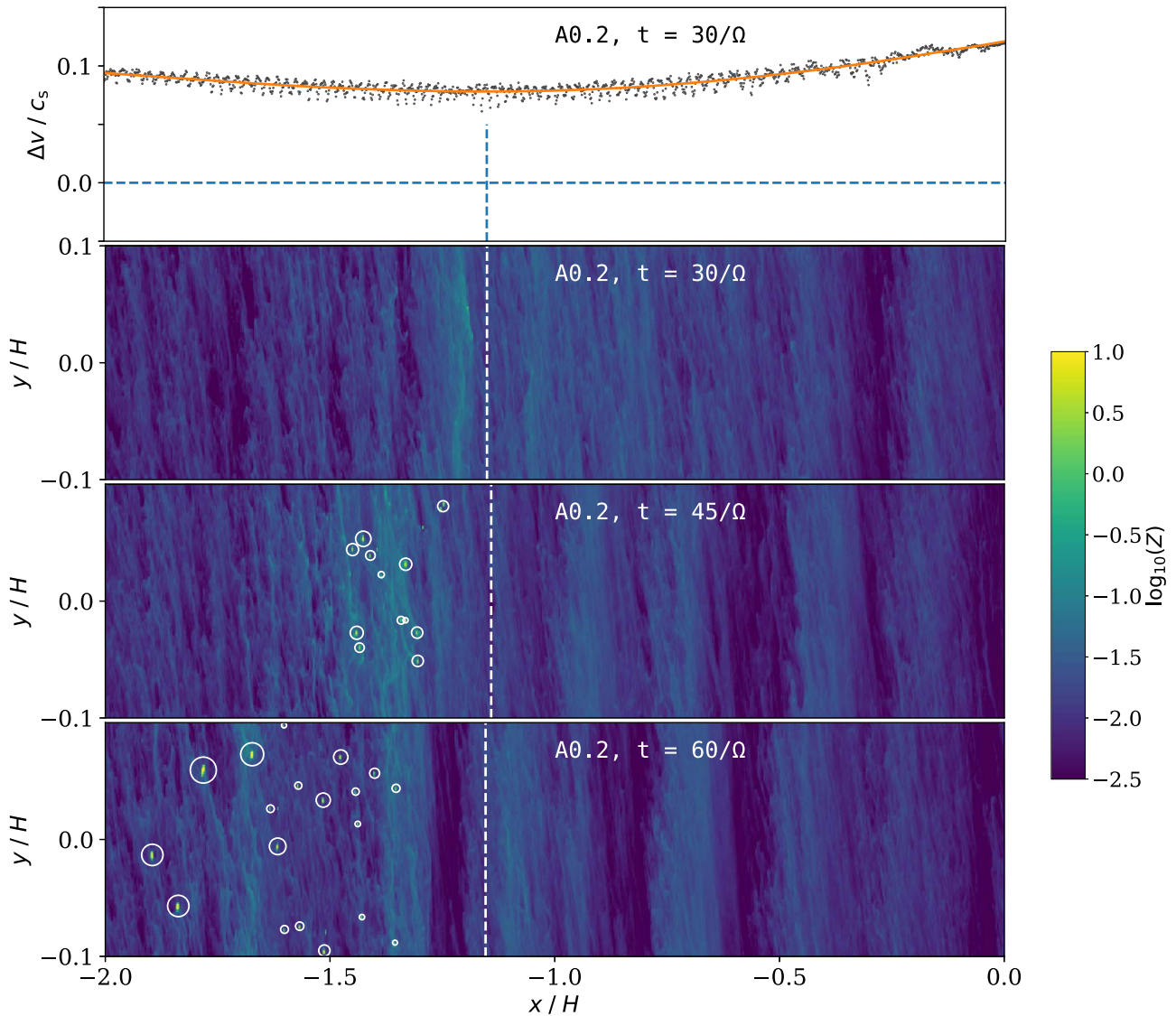


Figure 5. Snapshots of model A0.2 at the time when particle clumps form. Top: the black dots show the azimuthally averaged value of the headwind at $t = 25/\Omega$. The orange line corresponds to the same data as the black dots, but averaged over radially nearby points. The vertical dashed line marks the location where the orange line reaches its minimum value. Bottom three panels: snapshots of the column dust-to-gas ratio $Z = \Sigma_p/\Sigma$. White circles mark the location of bound clumps with $\rho_p \gg \rho_{\text{roche}}$.

of $\min(\Delta v)$ (snapshot $t = 30/\Omega$) and then drifts before bound clumps form.

5. Model A0.2 has $\min(\Delta v) \approx 0.08c_s$ at $t = 30/\Omega$. If A0.2 is indeed a marginal case, then $\Delta v \approx 0.08c_s$ may be close to the critical value needed for a pressure bump to trigger planetesimal formation by the SI.

5.4. Streaming or Gravitational Instability?

Our next experiment is designed to confirm whether the self-gravitating particle clumps in our simulations were truly the result of the SI, or whether GI induced by pure concentration in the bump is responsible. The SI is a radial convergence of particle drift caused by the particle-on-gas feedback (see Section 1). Therefore, we ran a simulation, `NoFeedback`, where we completely removed the particle feedback. This model has a bump amplitude of $A = 0.8$, so that it has a true particle trap (i.e., headwind $\Delta v = 0$) to maximize the particle concentration.

Figures 3 and 8 show that removing the particle feedback significantly delays the particle accumulation, as well as planetesimal formation, even in a simulation designed to trap particles. The panels of Figure 8 show 2D plots from runs A0.2–A0.8 and `NoFeedback` at a time near their peak particle density. The differences in the filamentary structure show that the `NoFeedback` run is dominated by very different physical processes. Runs A0.2–A0.8 show the wide filaments with complex substructure that are characteristic of the SI. The filaments in run `NoFeedback` are much narrower, are far more closely spaced, and do not have nearly as much substructure. Even if we compare `NoFeedback` to A0.8 (the run with trapping *and* feedback), there is a noticeable difference in the structure and sizes of formed clumps. Ultimately, these considerations strongly imply that it is the SI and not pure GI due to concentration that gives rise to planetesimal formation in pressure bumps.

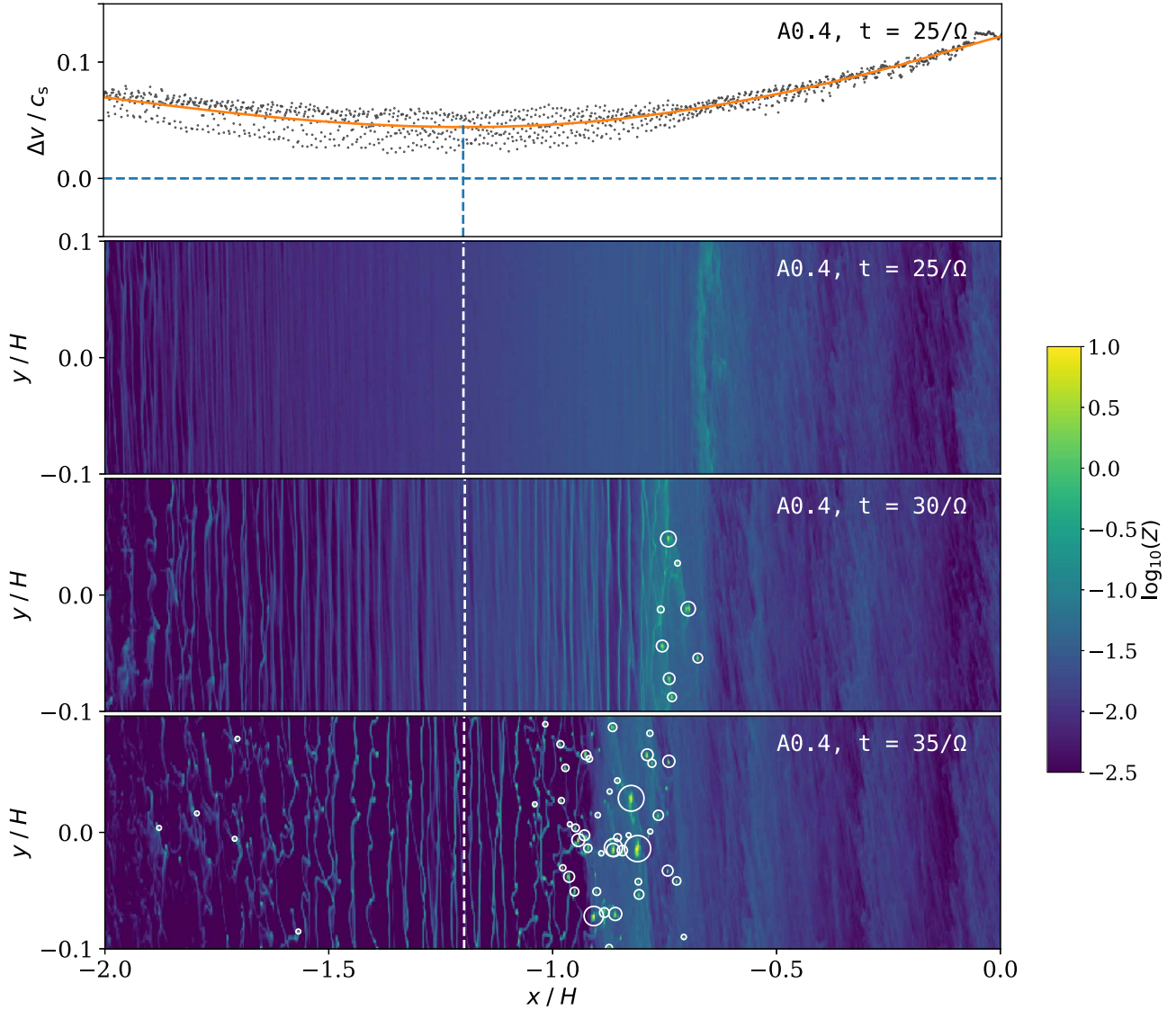


Figure 6. Snapshots of model A0.4 at the time when particle clumps form. Top: the black dots show the azimuthally averaged value of the headwind at $t = 25/\Omega$. The orange line corresponds to the same data as the black dots, but averaged over radially nearby points. The vertical dashed line marks the location where the orange line reaches its minimum value. Bottom three panels: snapshots of the column dust-to-gas ratio $Z = \Sigma_p/\Sigma$. White circles mark the location of bound clumps with $\rho_p \gg \rho_{\text{roche}}$.

5.5. Small Particles and Resolution Limit

In the case of millimeter-sized particles it appears that it may not be possible for a Rossby-wave-stable bump to trigger planetesimal formation by the SI. Figure 9 zooms into the two runs with millimeter-sized particles and extends the range of the time integration. Because the high-resolution run closely follows the low-resolution run, it appears that at least the bulk behavior of the millimeter-sized particles is mostly resolved. We extended `lores.1mm` to $t = 250\Omega^{-1}$ and only observed slow gradual growth of particle density. Simple linear extrapolation suggests that particles will reach the Roche density ($\rho_{\text{roche}} = 45$) at around $t_{\text{roche}} \sim 9000\Omega^{-1}$. For comparison, the radial drift timescale (using Equations (7) and (18)) is

$$t_{\text{drift}} \sim \frac{v_{\text{drift}}}{r} \sim 2270\Omega^{-1}. \quad (32)$$

Since $t_{\text{drift}} \ll t_{\text{roche}}$, these runs suggest that millimeter-sized particles may never reach the Roche density. The most important question now is whether this result reflects physical

reality or is merely a numerical limitation of our simulations. Specifically, it is possible that neither of these runs had a sufficiently high resolution to resolve the fastest-growing modes of the SI. In the SI, the fastest-growing modes are those that satisfy the epicyclic resonant condition (Squire & Hopkins 2020)

$$\mathbf{k} \cdot \mathbf{w}_s = \hat{k}_z \Omega, \quad (33)$$

where $\mathbf{k} = (k_x, 0, k_z)$ is the wavenumber, \mathbf{w}_s is the dust drift velocity with respect to the gas, and $\hat{k}_z = k_z/k$. Since $\mathbf{w}_s \approx -2\pi\eta v_k \hat{\mathbf{x}}$ (Nakagawa et al. 1986), the fastest-growing mode has wavelength

$$\lambda \approx -4\pi\tau\eta r \frac{k_x}{k_z}. \quad (34)$$

For our disk model at 50 au, and assuming the minimum value of η in the bump, we get $\lambda/H \approx 0.72\tau|k_x/k_z|$ for $A = 0.2$. Therefore, the resolution required to resolve the fastest-

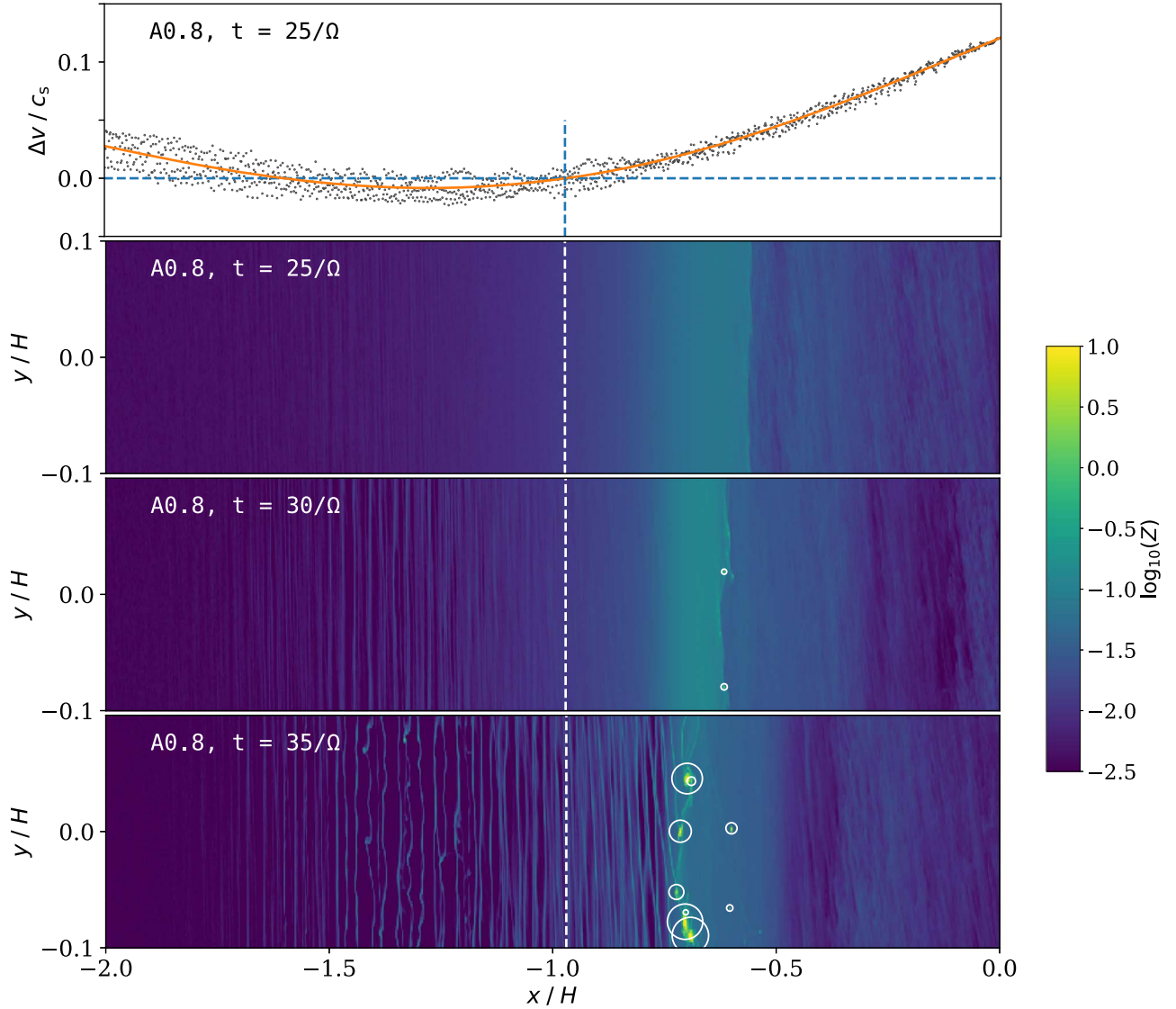


Figure 7. Snapshots of model A0.8 at the time when particle clumps form. Top: the black dots show the azimuthally averaged value of the headwind at $t = 25/\Omega$. The orange line corresponds to the same data as the black dots, but averaged over radially nearby points. The vertical dashed line marks the location where the orange line reaches its minimum value. Bottom three panels: snapshots of the column dust-to-gas ratio $Z = \Sigma_p/\Sigma$. White circles mark the location of bound clumps with $\rho_p \gg \rho_{\text{roche}}$.

growing mode of the SI is inversely proportional to the particle size. Our *hires.1mm* model has a resolution of $H/\Delta x = 640$, and *lores.1mm* has $H/\Delta x = 320$. If we let $|k_x/k_z| = 1$, then $\lambda/\Delta x \approx 3-6$. In other words, we should be able to resolve the fastest-growing mode if $|k_z| \leq |k_x|$, though given the low value of $\lambda/\Delta x$, this could be marginal.

It is worth keeping in mind that Equation (33) only applies for local solid-to-gas ratios less than unity. We find that 98.9% of the particle mass at the end of the *lores.1mm* is in regions where $\rho_p/\rho < 1$. Thus, the majority of our simulation domain should be susceptible to the $\rho_p/\rho < 1$ limit of the SI (Squire & Hopkins 2020). Furthermore, as pointed out in both Squire & Hopkins (2020) and the original work by Youdin & Goodman (2005), the condition $\rho_p/\rho > 1$ is generally seen as the criterion for the existence of faster-growing SI modes (i.e., growth rates dramatically increase above the $\rho_p/\rho = 1$ value). Whether it is possible for this fast-growing SI to be fully manifested in only 1.1% of our simulation (in terms of solid-to-gas ratio) is not entirely clear. Regardless, the fact that most of the particle mass

in *lores.1mm* falls within the $\rho_p/\rho < 1$ regime and that the fastest unstable SI modes are resolved by $\sim 3-6$ grid cells suggests that we might be able to see at least some indication of exponential SI growth; however, we do not.

We have also calculated the local-particle-density-weighted average of Z and τ for *lores.1mm*, as shown in Figure 10. At first blush, it appears that the simulation has reached the region where it should be unstable to the SI (according to the criterion of Yang et al. 2017). However, the SI criterion of Yang et al. (2017) was computed with a headwind parameter of $\Pi = 0.05$, whereas our simulations have $\Pi = 0.12$. Lower headwind is known to facilitate particle concentration by the SI (Bai & Stone 2010b), and thus it is possible that the Yang et al. (2017) criterion would be pushed toward higher Z values for our larger Π value. If, indeed, the critical Z for $\Pi = 0.12$ is larger than that reached in our simulation, that would explain the lack of strong clumping (and thus planetesimal formation).

Ultimately, to resolve these issues of the SI and its ability to produce planetesimals, we will need to carry out higher-

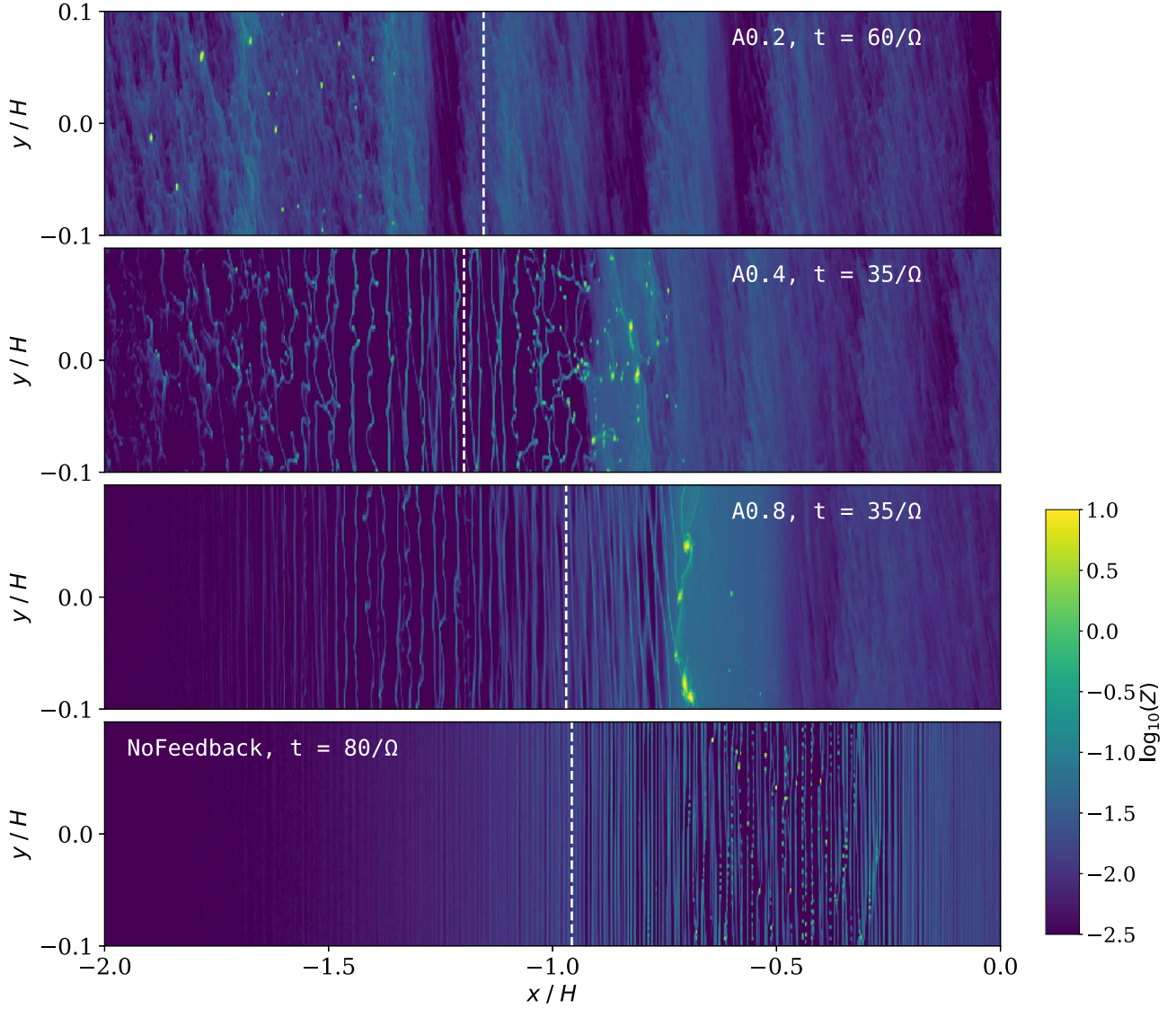


Figure 8. Snapshots of the column dust-to-gas ratio ($Z = \Sigma_p/\Sigma$) at the time that bound particle clumps form in models A0.2–A0.4 and NoFeedback. Notice the difference between the thick filaments formed in runs where the SI is active (A0.2–A0.4) and a model where planetesimals can only form by GI. Notice also that, even with a particle trap, GI takes longer to form planetesimals than the SI. Therefore, we find that the SI (and not GI) is the mechanism responsible for forming planetesimals in runs A0.2–A0.8.

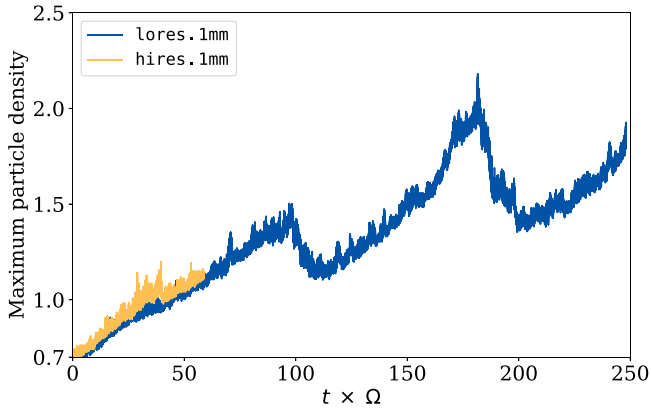


Figure 9. Maximum particle density (in code units) vs. time for the two runs with millimeter-sized particles. The high-resolution run closely follows the low-resolution one, which displays slow growth. At the present growth rate, millimeter-sized runs may not reach the Roche density until $t \sim 9000 \Omega^{-1}$, which is much longer than the particle drift timescale.

resolution simulations that explore a larger area of the parameter space. Given the rich physics associated with centimeter-sized particles and pressure bumps, which is the focus of this paper, we defer such work to a future publication.

5.6. Resilience of Particle Filaments

One unexpected result is that all of our simulations—including those that did not form planetesimals—consistently formed particle filaments. Moreover, the filaments form everywhere and are not restricted to the vicinity of the pressure bump. Figure 11 shows a 2D view of some of the filaments in A0.1. Figure 12 shows the dust density profile for snapshots of two runs that did not form planetesimals (lores.1mm and A0.1), along with our fiducial run (A0.2). This is important because the traditional clumping criteria of Carrera et al. (2015) and Yang et al. (2017) would predict that these regions of the box *should not be able to form particle clumps*. The dust-to-gas ratio at the edges ($Z \sim 0.01$) is far too small for the SI to be efficient—especially for lores.1mm ($\tau \sim 10^{-2}$). Yet

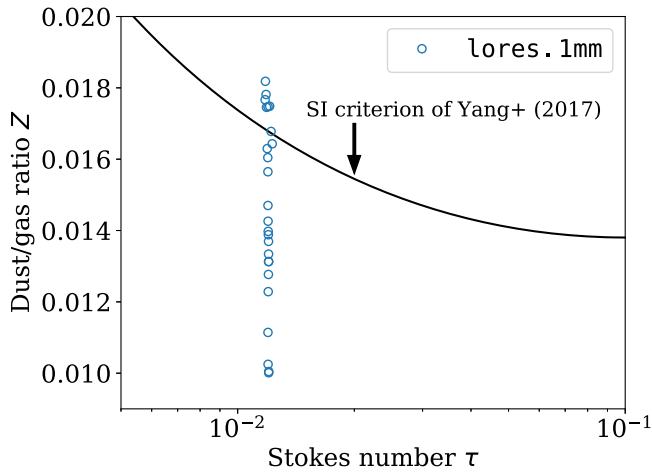


Figure 10. The black curve shows the SI criterion of Yang et al. (2017); disk conditions above the black curve are thought to be conducive to the SI. The blue circles mark the average dust-to-gas ratio Z (calculated as described in the main text) and Stokes number τ for run `lores.1mm`, computed in intervals of 10^{-1} .

filaments form. Evidently, clumping criteria obtained from small shearing box simulations may not generalize to large slices of the disk.

We find that the pressure bump does not *cause* the formation of SI filaments; rather, it causes filaments to become *denser* when they pass through the bump. This effect is hard to see on a still image, but it is most visible in the bottom panel (`A0.2`) of Figure 12—note that the filaments in the planetesimal formation region ($-2 \lesssim x/H \lesssim 0$) have a much higher peak than those near the edges of the box.

5.7. Feedback and Reinforcement

The same particle feedback that is responsible for the SI also disrupts the pressure bump. As particles push back on the gas, they dissipate the pressure bump and alter its shape and location. So far in this work we have invoked an unspecified external force (such as a planet) to regularly reinforce the pressure bump (Section 4.3). In this section we explore how the pressure bump responds to particle feedback in the absence of external reinforcement.

Simulations `R0.2` and `R0.8` begin with a fully formed pressure bump with amplitudes of $A=0.2$ and 0.8 . At the beginning of each simulation the pressure bump is in geostrophic balance, meaning that in the absence of particle feedback the bump would be sustained indefinitely. Figure 13 shows the midplane gas density for `R0.2` and `R0.8`. Over the first $\Delta t \sim 10 \Omega^{-1}$ there is very little change because the particle density (and thus particle feedback) is initially low. For the first $t \sim 10 \Omega^{-1}$ the particles sediment (Figure 3). At that moment, the particle density at the midplane is high enough to alter the azimuthal velocity of the gas, and, without reinforcement, the shape of the bump begins to change.

Figure 13 shows how the pressure bump is gradually dissipated by particle feedback, and the shape of the bump visibly changes over the scale of $\sim 10 \Omega^{-1}$. While that happens, the bump also drifts inward and gains a negative skew. We were surprised that runs `R0.2` and `R0.8` have very similar bump evolution, despite the bumps having very different sizes. Our interpretation is that, while a small pressure bump may, in principle, be more vulnerable to disruption by

particle feedback, the amount of feedback is proportional to the particle concentration, which itself is driven by the bump size. In other words, it appears that pressure bump dissipation by particle feedback is a somewhat self-similar process.

The negative skew in Figure 13 is important because the starward side of the bump (i.e., interior to the peak) is also where particles would normally concentrate to form planetesimals. We find that in `R0.2` and `R0.8` planetesimal formation is less efficient than in `A0.2` and `A0.8`, respectively. Inspired by Lenz et al. (2019), we define the planetesimal formation efficiency ϵ by

$$\epsilon \approx f \cdot \frac{L_x/T}{v_r}, \quad (35)$$

where f is the fraction of the particle mass at the end of the simulation that will very likely be converted into planetesimals (we chose particles in grid cells with $\rho_p > 10^3 \rho_{\text{roche}}$), L_x is the length of the simulation box, T is the simulation time, and v_r is the *unperturbed* radial drift speed. In other words, the effect the pressure bump has on v_r is included in ϵ .⁹

The intuitive explanation for Equation (35) is that if $v_r = L_x/T$, that means that, in principle, the simulation has run long enough to allow every particle a chance to pass through the pressure bump and potentially become a planetesimal, and in that case f is a good estimate of the final planetesimal formation efficiency. In practice, none of our simulations run this long, so we attempt to extrapolate. In other words, ϵ is a simple extrapolation of f ; it is a rough estimate of the planetesimal formation efficiency in a disk with bumps separated by distance L_x where every particle gets a chance to pass through the pressure bump once.

One salient limitation of Equation (35) is that this kind of extrapolation is invalid in runs where particles can drift outward. Therefore, we do not compute ϵ for runs `A0.8` and `R0.8`. Table 2 shows ϵ and f for all the runs that produced bound clumps.

Figure 14 shows the maximum particle density for `R0.2` and `R0.8`. Run `R0.2` forms planetesimals much later than `A0.2`. Run `R0.8` crosses the Roche density sooner than `A0.8`, partly aided by a bump that is already formed, but the density growth is slower and the peak density is reached later than in `A0.8`.

The relevance of the comparison with `R0.2` and `R0.8` is limited because it seems unlikely that a pressure bump would form but then have no mechanism to reinforce it. A more physically realistic scenario would be to model a bump that develops with a reinforcement timescale longer than $t_{\text{reinf}} = 1 \Omega^{-1}$. We will explore that idea in a future investigation.

Our finding that particle feedback significantly alters the pressure bump is in conflict with Onishi & Sekiya (2017). They found that particles sediment to a thin layer so that most of the gas in the bump is unaffected by the back-reaction. The discrepancy cannot be due to the box size since our box is in fact taller ($z_{\text{max}} = 0.2H$ vs. $0.125H$) and our particles are larger ($\tau \approx 0.12$ vs. 0.01) than theirs. Other differences between `R0.2` and Onishi & Sekiya (2017) include the background pressure gradient Π , the presence of an azimuthal direction, and boundary conditions—they use a reflecting boundary in the vertical direction, whereas we use an open boundary with

⁹ We did one test where we defined v_r as the average particle drift rate across the entire simulation (`A0.2`), and the value was nearly identical.

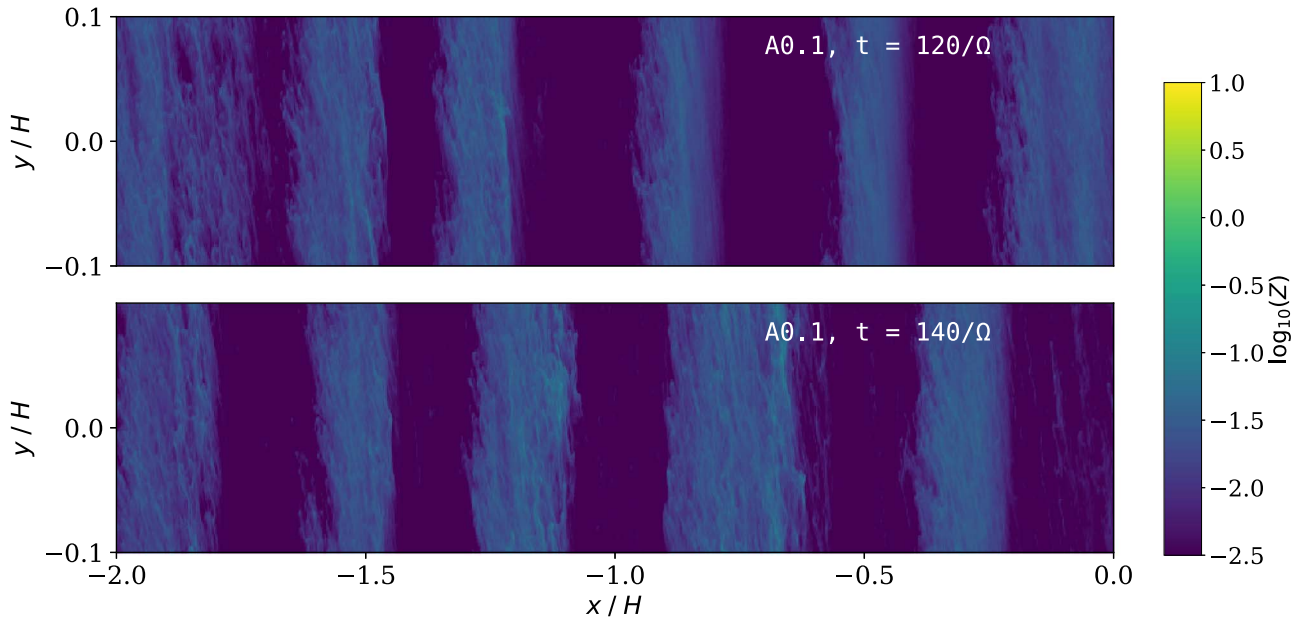


Figure 11. Snapshots of the column dust-to-gas ratio $Z = \Sigma_p/\Sigma$ in model A0.1. The simulation does not form planetesimals, but particle filaments are clearly visible. Filaments like these are seen across the entire simulation box even in models that do not form planetesimals (see Figure 12).

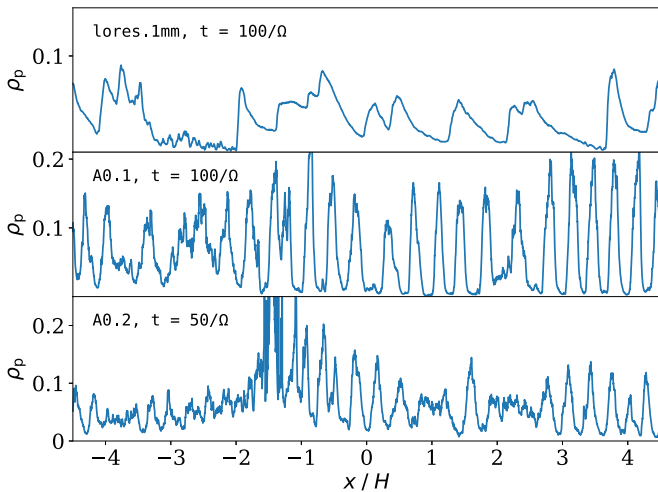


Figure 12. Mean particle density across the shearing box for three sample simulations in code units, where the gas density is $\rho \approx 1$. Even simulations that do not form planetesimals—top two panels—consistently form particle filaments. Furthermore, particle filaments are not restricted to the vicinity of the pressure bump ($|x/H| \lesssim 2$). Rather, filaments form everywhere, and as they pass through the bump, the filament density increases (e.g., bottom panel).

regular density rescaling to conserve mass. It is possible that some of these might be responsible for the different results.

5.8. Characteristic Particle Concentration

Figure 15 shows a histogram of the particle density for runs A0.2, A0.8, R0.2, and R0.8. It shows the fraction of the particle mass in each density interval. Perhaps the most interesting feature of this graph is that it clearly shows at least two characteristic density scales that are present in all simulations:

- (1) The bulk of the particle mass is always inside a dominant mode in the vicinity of $\rho_p \sim 1$, where the particle density is in the same magnitude range as the gas density. This is likely the characteristic density scale of SI filaments.

- (2) There is always a second mode in the vicinity of $\rho_p \sim 10^3-10^4 \gg \rho_{\text{roche}}$, where the physics is clearly dominated by self-gravity. The runs with bump reinforcement (A0.2, A0.8) have higher ρ_p than their un-reinforced counterparts. We shall return to this point at the end of this section. Note that that mode is still present for R0.2, though it is somewhat difficult to see in the figure, as it contains only 1% of the particle mass.

Finally, run A0.8 has a third major mode (3) near $\rho_p \sim 40$ that does not seem to be present in the other runs. This points to an additional structure that is likely associated with the particle trap (R0.8 begins with a particle trap too, but it moves as the bump is deformed). Figure 16 shows a close-up view of the planetesimal-forming region of run A0.8. There is indeed an additional layer of structure that we do not generally see in other runs: a network of very thin and dense particle filaments, often connecting particle clumps to one another. Similar filaments can be seen in A0.4 at $t = 30/\Omega$ (Figure 6), but they appear to be a transient feature that is quickly destroyed by Keplerian shear. This filamentary structure can only last if the bound clumps form in nearly the same orbit, as is the case in A0.8.

The bound clumps in runs with bump reinforcement are more massive than their un-reinforced counterparts. This likely explains the higher characteristic density in A0* versus R0* (Figure 15). Quantitatively, the mean clump mass in A0.8 (1.58% of the total particle mass) is 22 times larger than that of R0.8 (0.07%), and the mean clump mass in A0.2 (0.41%) is 9 times larger than that of R0.2. In addition, A0.8 stands out because it is dominated by a handful of very massive clumps—it has four clumps with 3.4% of the total particle mass and five smaller clumps with 0.1% of the particle mass. Run A0.2 forms 19 clumps with a more equal distribution of mass. It is possible that the presence of filaments (as discussed above) and the slower radial drift (see Figure 7) in A0.8 conspire to continually feed the clumps already formed, leading to several very massive clumps.

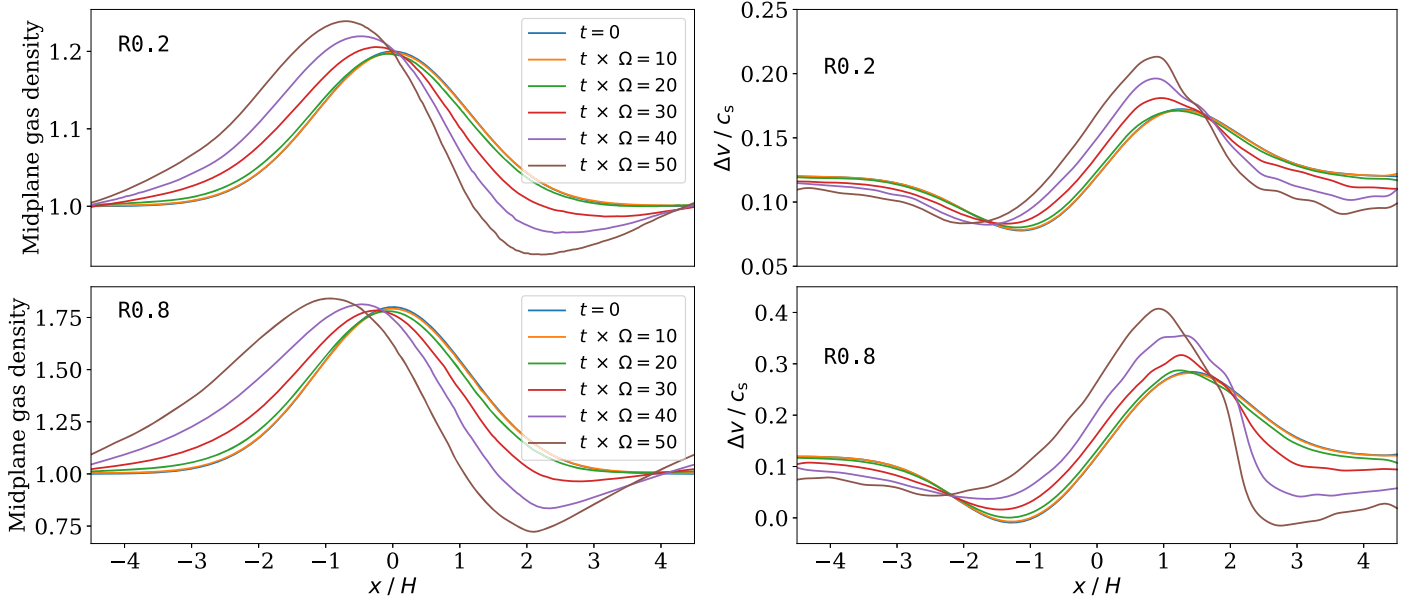


Figure 13. Left: snapshots of the midplane gas density profile (in code units) for two simulations with no pressure bump reinforcement. Right: azimuthally averaged headwind for the same snapshots. The runs begin with a fully formed pressure bump with amplitude $A = 0.2$ (top) or 0.8 (bottom) in geostrophic balance. In the absence of particle feedback, the pressure bump would survive indefinitely. With particles present, particle feedback gradually dissipates the bump, skews the bump toward the star, pushes the peak inward, and distorts the gas velocity profile. This occurs over $\sim 50 \Omega^{-1}$, and many features are largely independent of the bump size.

Table 2

Planetesimal Formation Efficiency ϵ (Equation (35)) and Fraction of the Particle Mass in Bound Clumps f for Every Model That Made Bound Clumps

Model	Planetesimal Formation Efficiency ϵ	f
A0.2	0.42	0.08
A0.4	0.87	0.10
A0.8	...	0.15
R0.2	9.6×10^{-3}	3.2×10^{-3}
R0.8	...	0.11

Note. Lack of reinforcement in R0.2 and R0.8 substantially reduces the formation efficiency, especially at low amplitude (R0.2). There is no ϵ for A0.8 and R0.8 because Equation (35) is not applicable to a model where particles can drift outward.

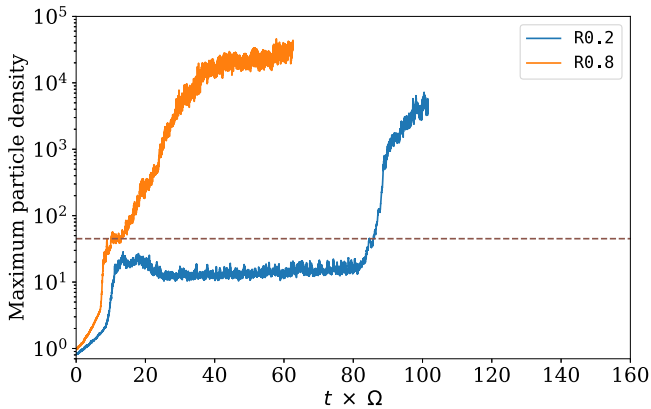


Figure 14. Maximum particle density (in code units) vs. time for the two runs with no bump reinforcement. The dashed line marks the Roche density. Despite the lack of reinforcement, both runs reach the Roche density and form gravitationally bound clumps, though with a notable delay in the case of R0.2 (compare with Figure 3).

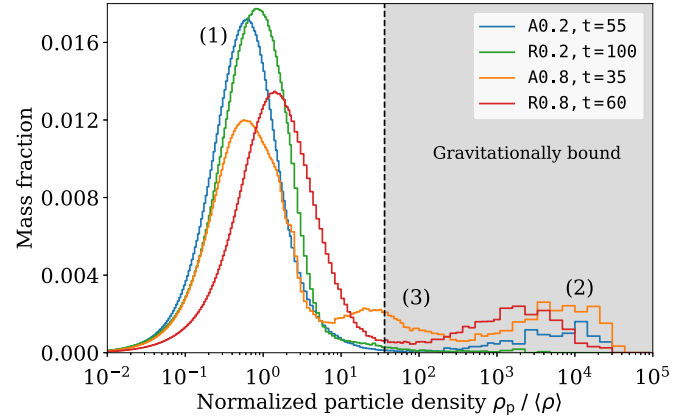


Figure 15. Histogram of the particle density near the end of four simulations. Two runs have a bump amplitude of $A = 0.2$ (A0.2 and R0.2), and two have $A = 0.8$. In two runs, the pressure bump is reinforced on a timescale of $t_{\text{reinf}} = 1 \Omega^{-1}$ (A0.2 and A0.8), and in the other runs the bump is not reinforced at all (R0.2 and R0.8). The main mode (1) shows that most of the particle mass is in regions with $\rho_p \sim 1$ (i.e., comparable to the gas density) and is probably associated with SI filaments. All runs have a second mode (2) at $\rho_p \sim 10^4$, probably dominated by self-gravity. Run A0.8 has another mode (3) at $\rho_p \sim 40$, likely caused by a combination of the particle trap and the SI.

6. Uncertainties and Future Work

Our work is subject to a number of uncertainties and limitations, both numerical and physical in nature. First, as with many previous studies of streaming-induced planetesimal formation, our FFT-based gravity solver halts collapse at the grid scale, which prevents our planetesimals from collapsing to scales of ~ 100 km. While this limitation restricts what we can learn about the physical properties of planetesimals, it likely does not play a significant role (if any at all) in whether or not planetesimals form, as well as how and when they form, which are the primary questions addressed in this work.

Furthermore, as pointed out in Section 4.4, the radial extent of our domain stretches the validity of the local approximation.

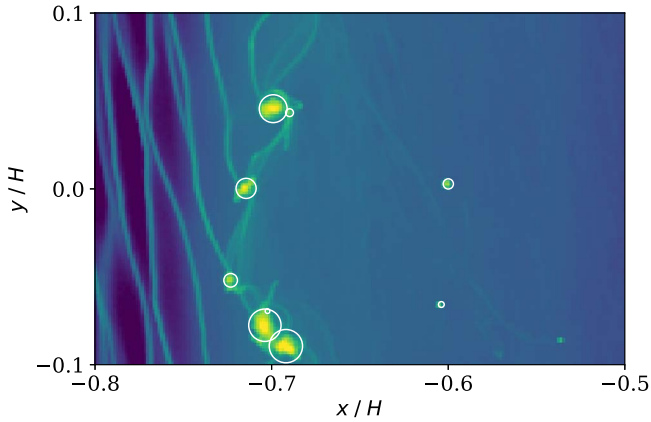


Figure 16. Column dust-to-gas ratio ($Z = \Sigma_p/\Sigma$) for a narrow slice of model A0.8 near the end of the simulation. Unique to this run is another prominent structure—a network of thin, dense filaments, often connecting bound particle clumps to one another. This structure is associated with the third mode (3) in Figure 15. The color bar employed is the same as the previous snapshots (Figures 5–8).

However, as we also discussed above, the particle enhancement and subsequent growth of the SI occur on scales $\ll L_x$. In the absence of global simulations that incorporate the same physics (which are not yet developed), such extended local simulations will suffice.

An additional limitation associated with this setup is the approach used to simulate a pressure bump: the pressure bump is artificially induced and maintained via Newtonian relaxation toward a state of geostrophic balance. While this configuration gives us explicit control over the relevant bump parameters (e.g., amplitude, reinforcement timescale), and in that sense can be seen as a strength, future simulations that include bump-inducing mechanisms (e.g., planets, magnetically induced zonal flows) will be necessary in order to fully test the results explorably with our current setup.

Additionally, most of our simulations assume centimeter-sized particles. In regions where drift-limited particle growth occurs (e.g., Birnstiel et al. 2012), these particles may be too large. However, the simulations carried out here provide invaluable insight even in such a limit, and our tentative result that millimeter-sized particles do not produce strong clumping strongly motivates future studies to determine whether or not this is indeed the case.

Finally, in this same vein, a recent result by Krapp et al. (2019) shows that the linear growth of the SI may not converge with increasing number of particle sizes. If such nonconvergence carries over to the nonlinear regime in the absence of a pressure bump, studies *with* a pressure bump may be crucial, as such bumps serve as natural sites to spatially separate particles of different sizes (e.g., smaller τ particles will be less concentrated within the bump in the presence of turbulent diffusion).

7. Summary and Conclusions

We conducted shearing box simulations with ATHENA in order to explore the formation of planetesimals in a pressure bump similar in size to those observed by ALMA in nearby protoplanetary disks (e.g., Huang et al. 2018). Previous numerical work on the SI has relied on simulations with idealized conditions, such as a large initial solid-to-gas ratio Z , that are “rigged” to be more conducive to planetesimal

formation. Our work presents the first set of simulations that show that planetesimal formation is possible (and even quite robust) under conditions likely to be realized in protoplanetary disk systems, namely, $Z=0.01$ (comparable to the solar nebula) and in the presence of largely axisymmetric (but RWI-stable) pressure bumps that have properties similar to those observed by ALMA. Our main conclusions are as follows:

1. Planetesimal formation inside a pressure bump is a robust process that does not require a particle trap and can occur even for moderately low amplitude pressure bumps that are more likely to be RWI stable. The local enhancement in particle density that arises from particles drifting through the pressure bump is sufficient to kick-start the SI and produce planetesimals.
2. As a corollary, planetesimal formation occurs in filaments that are continually drifting inward past the pressure bump maximum; planetesimals are formed inward (i.e., closer to the star) of the pressure bump that initiated their growth.
3. These planetesimals are formed via the SI and not direct gravitational collapse due to concentration from the pressure bump itself.
4. Particle filaments are a much more robust process than traditional clumping criteria suggest (Carrera et al. 2015; Yang et al. 2017). Filaments form across the entire box, even in simulations that do not form planetesimals and even in regions where the clumping criterion is not satisfied. Evidently, the clumping criterion from small box simulations does not seem to generalize to larger scales.
5. Bound particle clumps from simulations with a particle trap (run A0.8) are fewer in number, less radially dispersed, and more massive.
6. In the absence of reinforcement, feedback from the particles distorts the shape of the pressure bump. Nonetheless, planetesimals still form, albeit at a lower efficiency.
7. The critical bump amplitude needed to trigger planetesimal formation (for the parameter combinations considered here) appears to be higher than 10% and below 20%. This value may be different in the inner disk, where the background pressure gradient is less steep, and it may also be different for small particles.
8. For the resolution employed here, millimeter-sized particles do not produce planetesimals in pressure bumps. Given that at large radial distances from the star drift-limited particle growth limits particle sizes to millimeters (see Birnstiel et al. 2012), this result, if it holds at higher resolutions, suggests that planetesimal formation is not possible within the drift-limited regions of protoplanetary disks.

Taken together, these results have one underlying implication: planetesimal formation in pressure bumps from centimeter-sized particles occurs via the SI and is extremely robust. While future work to study different bump reinforcement timescales will be required to verify this result, the fact that amplitudes of only $\sim 10\%$ – 20% are needed to initiate the SI points to a wide variety of conditions under which planetesimals can form.

The most studied mechanism for forming pressure bumps is the carving of gaps by planets in protoplanetary disks. As the planet exchanges angular momentum with the gas, a gap opens up, which ultimately leads to a pressure increase (a “bump”) moving away from the gap. Indeed, there is now observational evidence that the gaps observed in many Class II sources (e.g., Huang et al. 2018) are actually the result of planets (Pinte et al. 2018; Teague et al. 2019). Of course, if planetesimals form in these planet-induced bumps, they would represent a *later* generation of planetesimals, and not those that formed the first generation of planets.

Saving us from the pitfalls of this “chicken or the egg” type paradox (i.e., how did the first generation of planetesimals form?), there is both theoretical and observational evidence that pressure bumps can form in even younger systems and without the aid of already-formed planets. In terms of observations, both HL Tau (likely transitioning from Class I to Class II; ALMA Partnership et al. 2015) and GY 91 (a Class I system; Sheehan & Eisner 2018) contain dust rings that indicate the presence of pressure bumps. While such observations do not rule out the planet hypothesis for bump formation, it motivates the consideration of alternative mechanisms, lest planet formation in these very young systems is far enough along that they are already able to carve substantial gaps.

On the theoretical side, a large number of alternative mechanisms have been proposed to generate bumps and rings in disks. For example, many studies have explored the evolution of magnetically induced zonal flows and related phenomena (e.g., Lyra et al. 2008; Johansen et al. 2009; Dzyurkevich et al. 2010; Uribe et al. 2011; Simon et al. 2012; Simon & Armitage 2014; Bai 2015; Suriano et al. 2018; Riols & Lesur 2019). While the exact amplitude of the pressure bumps induced by these processes depends on the particular setup (e.g., assumed magnetic field strength), it often exceeds $\sim 20\%$ (Dzyurkevich et al. 2010; Uribe et al. 2011; Bai 2015).

Furthermore, transitions between ionization regions can also generate pressure bumps. Dzyurkevich et al. (2010) showed that the inner edge of the ohmic dead zone (see Gammie 1996 for a description of the dead zone) may harbor a pressure bump much larger than 20%. Flock et al. (2015) carried out similar calculations and found that a pressure bump can form at the outer edge of the dead zone with sufficiently large amplitude as to halt radial drift of particles (though, consistent with our discussion above, this bump was unstable to the RWI).

Beyond these models, there are a number of other mechanisms that can produce pressure bumps in disks, many of which have not been characterized in terms of percentage of pressure variation. However, amplitudes of $\sim 10\%$ – 20% are not outrageously high; indeed, one can easily envision any number of mechanisms producing such modest amplitude fluctuations. Ultimately, the prevalence of ring structures, in both observational detections and mechanisms by which they can form, coupled with the results of this work, strongly indicates that planetesimal formation in pressure bumps is not only viable but also very likely commonplace.

We thank Hui Li, Jonathan Squire, Phil Armitage, Andrew Youdin, and Wlad Lyra for useful discussions and suggestions regarding this work. We also thank the referee for all the useful feedback that helped improve this manuscript. D.C. and J.B.S. acknowledge support from NASA under *Emerging Worlds* through grants 80NSSC18K0597 and 80NSSC19K0502. R.L.

acknowledges support from NASA under grant NNX16AP53H. The numerical simulations and analyses were performed on STAMPEDE 2 through XSEDE grant TG-AST120062.

Software: ATHENA (Stone et al. 2008; Bai & Stone 2010c; Simon et al. 2016), Julia (Bezanson et al. 2017), and Matplotlib (Hunter 2007).

ORCID iDs

Daniel Carrera  <https://orcid.org/0000-0001-6259-3575>
 Jacob B. Simon  <https://orcid.org/0000-0002-3771-8054>
 Rixin Li  <https://orcid.org/0000-0001-9222-4367>
 Katherine A. Kretke  <https://orcid.org/0000-0001-9601-878X>
 Hubert Klahr  <https://orcid.org/0000-0002-8227-5467>

References

- Abod, C. P., Simon, J. B., Li, R., et al. 2019, *ApJ*, 883, 192
 ALMA Partnership, Brogan, C. L., Pérez, L. M., et al. 2015, *ApJL*, 808, L3
 Andrews, S. M., Huang, J., Pérez, L. M., et al. 2018, *ApJL*, 869, L41
 Bai, X.-N. 2015, *ApJ*, 798, 84
 Bai, X.-N., & Stone, J. M. 2010a, *ApJ*, 722, 1437
 Bai, X.-N., & Stone, J. M. 2010b, *ApJL*, 722, L220
 Bai, X.-N., & Stone, J. M. 2010c, *ApJS*, 190, 297
 Bezanson, J., Edelman, A., Karpinski, S., & Shah, V. B. 2017, *SIAMR*, 59, 65
 Birnstiel, T., Klahr, H., & Ercolano, B. 2012, *A&A*, 539, A148
 Carrera, D., Gorti, U., Johansen, A., & Davies, M. B. 2017, *ApJ*, 839, 16
 Carrera, D., Johansen, A., & Davies, M. B. 2015, *A&A*, 579, A43
 Colella, P. 1990, *JCoPh*, 87, 171
 Colella, P., & Woodward, P. R. 1984, *JCoPh*, 54, 174
 Drazkowska, J., & Alibert, Y. 2017, *A&A*, 608, A92
 Dzyurkevich, N., Flock, M., Turner, N. J., Klahr, H., & Henning, T. 2010, *A&A*, 515, 70
 Eriksson, L. E. J., Johansen, A., & Liu, B. 2020, *A&A*, 635, A110
 Flock, M., Ruge, J. P., Dzyurkevich, N., et al. 2015, *A&A*, 574, A68
 Gammie, C. F. 1996, *ApJ*, 457, 355
 Gardiner, T. A., & Stone, J. M. 2005, *JCoPh*, 205, 509
 Gardiner, T. A., & Stone, J. M. 2008, *JCoPh*, 227, 4123
 Gerbig, K., Murray-Clay, R. A., Klahr, H., & Baehr, H. 2020, *ApJ*, 895, 91
 Gundlach, B., & Blum, J. 2015, *ApJ*, 798, 34
 Güttler, C., Blum, J., Zsom, A., Ormel, C. W., & Dullemond, C. P. 2010, *A&A*, 513, A56
 Hawley, J. F., Gammie, C. F., & Balbus, S. A. 1995, *ApJ*, 440, 742
 Huang, J., Andrews, S. M., Dullemond, C. P., et al. 2018, *ApJL*, 869, L42
 Hunter, J. D. 2007, *CSE*, 9, 90
 Ida, S., & Guillot, T. 2016, *A&A*, 596, L3
 Johansen, A., Mac Low, M.-M., Lacerda, P., & Bizzarro, M. 2015, *SciA*, 1, 1500109
 Johansen, A., Oishi, J. S., Mac Low, M.-M., et al. 2007, *Natur*, 448, 1022
 Johansen, A., & Youdin, A. 2007, *ApJ*, 662, 627
 Johansen, A., Youdin, A., & Klahr, H. 2009, *ApJ*, 697, 1269
 Johansen, A., Youdin, A. N., & Lithwick, Y. 2012, *A&A*, 537, A125
 Johnson, B. M., Guan, X., & Gammie, C. F. 2008a, *ApJS*, 177, 373
 Johnson, B. M., Guan, X., & Gammie, C. F. 2008b, *ApJS*, 179, 553
 Kothe, S., Blum, J., Weidling, R., & Güttler, C. 2013, *Icar*, 225, 75
 Koyama, H., & Ostriker, E. C. 2009, *ApJ*, 693, 1316
 Krapp, L., Benítez-Llambay, P., Gressel, O., & Pessah, M. E. 2019, *ApJL*, 878, L30
 Lenz, C. T., Klahr, H., & Birnstiel, T. 2019, *ApJ*, 874, 36
 Li, H., Finn, J. M., Lovelace, R. V. E., & Colgate, S. A. 2000, *ApJ*, 533, 1023
 Li, R., Youdin, A. N., & Simon, J. B. 2018, *ApJ*, 862, 14
 Li, R., Youdin, A. N., & Simon, J. B. 2019, *ApJ*, 885, 69
 Lovelace, R. V. E., Li, H., Colgate, S. A., & Nelson, A. F. 1999, *ApJ*, 513, 805
 Lyra, W., Johansen, A., Klahr, H., & Piskunov, N. 2008, *A&A*, 479, 883
 Masset, F. 2000, *A&AS*, 141, 165
 Musiolik, G., & Wurm, G. 2019, *ApJ*, 873, 58
 Nakagawa, Y., Sekiya, M., & Hayashi, C. 1986, *Icar*, 67, 375
 Nesvorný, D., Li, R., Youdin, A. N., Simon, J. B., & Grundy, W. M. 2019, *NatAs*, 3, 808
 Nesvorný, D., Youdin, A. N., & Richardson, D. C. 2010, *AJ*, 140, 785
 Onishi, I. K., & Sekiya, M. 2017, *EP&S*, 69, 50

- Ono, T., Muto, T., Takeuchi, T., & Nomura, H. 2016, *ApJ*, 823, 84
- Ormel, C. W., & Cuzzi, J. N. 2007, *A&A*, 466, 413
- Pinte, C., Price, D. J., Ménard, F., et al. 2018, *ApJL*, 860, L13
- Riols, A., & Lesur, G. 2019, *A&A*, 625, A108
- Rosotti, G. P., Teague, R., Dullemond, C., Booth, R. A., & Clarke, C. J. 2020, *MNRAS*, 495, 173
- Schäfer, U., Yang, C.-C., & Johansen, A. 2017, *A&A*, 597, A69
- Schoonenberg, D., & Ormel, C. W. 2017, *A&A*, 602, A21
- Sheehan, P. D., & Eisner, J. A. 2018, *ApJ*, 857, 18
- Simon, J. B., & Armitage, P. J. 2014, *ApJ*, 784, 15
- Simon, J. B., Armitage, P. J., Li, R., & Youdin, A. N. 2016, *ApJ*, 822, 55
- Simon, J. B., Armitage, P. J., Youdin, A. N., & Li, R. 2017, *ApJL*, 847, L12
- Simon, J. B., Beckwith, K., & Armitage, P. J. 2012, *MNRAS*, 422, 2685
- Simon, J. B., Hawley, J. F., & Beckwith, K. 2011, *ApJ*, 730, 94
- Squire, J., & Hopkins, P. F. 2020, *MNRAS*, 498, 1239
- Stammler, S. M., Drazkowska, J., Birnstiel, T., et al. 2019, *ApJL*, 884, L5
- Stone, J. M., & Gardiner, T. A. 2010, *ApJS*, 189, 142
- Stone, J. M., Gardiner, T. A., Teuben, P., Hawley, J. F., & Simon, J. B. 2008, *ApJS*, 178, 137
- Suriano, S. S., Li, Z.-Y., Krasnopolsky, R., & Shang, H. 2018, *MNRAS*, 477, 1239
- Taki, T., Fujimoto, M., & Ida, S. 2016, *A&A*, 591, A86
- Teague, R., Bae, J., & Bergin, E. A. 2019, *Natur*, 574, 378
- Toomre, A. 1964, *ApJ*, 139, 1217
- Uribe, A. L., Klahr, H., Flock, M., & Henning, T. 2011, *ApJ*, 736, 85
- Wada, K., Tanaka, H., Suyama, T., Kimura, H., & Yamamoto, T. 2009, *ApJ*, 702, 1490
- Wahlberg Jansson, K., & Johansen, A. 2014, *A&A*, 570, A47
- Weidenschilling, S. J. 1977, *MNRAS*, 180, 57
- Weidling, R., Güttler, C., & Blum, J. 2012, *Icar*, 218, 688
- Whipple, F. L. 1972, in *From Plasma to Planet*, ed. A. Elvius (New York: Wiley), 211
- Yang, C. C., Johansen, A., & Carrera, D. 2017, *A&A*, 606, A80
- Youdin, A., & Johansen, A. 2007, *ApJ*, 662, 613
- Youdin, A. N., & Goodman, J. 2005, *ApJ*, 620, 459
- Zsom, A., Ormel, C. W., Güttler, C., Blum, J., & Dullemond, C. P. 2010, *A&A*, 513, A57